

Title:

Intravital 3D bioprinting

Authors: Anna Urciuolo, Ilaria Poli, Luca Brandolino, Paolo Raffa, Valentina Scattolini, Cecilia Laterza, Giovanni Giuseppe Giobbe, Elisa Zambaiti, Giulia Selmin, Michael Magnussen, Laura Brigo, Paolo De Coppi, Stefano Salmaso, Monica Giomo, Nicola Elvassore*

*Correspondence to: n.elvassore@ucl.ac.uk

Abstract:

Despite the tremendous technical advancements in 3D bioprinting, the concept of fabricating 3D structures and functional tissues directly in live animals remains a visionary challenge. We show that 3D cell-laden hydrogels can be efficiently bioprinted across tissues and within tissues of living animals.

We developed photo-sensitive polymers that allow *in vitro* and *in vivo* fabrication of hydrogels into pre-existing structures, by bio-orthogonal two-photon cycloaddition and crosslinking at wavelengths longer than 850 nm, without byproducts. By this technique, that we name intravital 3D bioprinting, after injection of these polymers *in vivo* it is possible to fabricate complex 3D structures inside tissues of living mice, including the dermis across epidermis, the skeletal muscle across epimysium or the brain across meninges. The use of commonly available multi-photon microscopes allows accurate (XYZ) positioning and orientation of bioprinted structures into specific anatomical sites. Finally, we show that intravital 3D bioprinting of donor muscle-derived stem cells allows *de novo* formation of myofibers in host animals. We envision that this strategy will offer an alternative *in vivo* approach to conventional bioprinting technology, holding great promises to substantially change the paradigm of 3D bioprinting for pre-clinical and clinical use.

Main Text:

3D printing is an additive process in which successive layers of materials are structured to generate 3D shapes. Such technology is being applied to enable rapid prototyping and manufacturing in industry, as well as production of personalized consumer products^{1,2}. Advanced systems have recently implemented layer-by-layer precise positioning of biomaterials, mainly hydrogels, as well as biochemicals and living cells into complex 3D functional tissues, thus progressing from 3D printing to 3D bioprinting³⁻⁶.

3D bioprinting aims at replicating the composition, mechanical properties and 3D architecture of biological tissues/organs for a large spectrum of biomedical applications. These include the generation of complex *in vitro* 3D models for drug discovery or biological studies, and the development of implantable functional living human constructs (biomaterials combined with cells) suitable for the restoration of tissue/organ function³⁻⁶. As for their clinical application, 3D living constructs are either incubated *in vitro* for maturation before implantation, or 3D bioprinted and then implanted *in vivo*³⁻⁸ through surgical procedures. Recently reported *in situ* 3D bioprinting has been limited to damaged areas of external and accessible loci such as skin^{9,10} or sites previously exposed by surgical procedure, such as bone¹¹ and cartilage¹². The conventional bioprinting approaches require direct access to printing sites and free XYZ spatial movements of the bioprinting head, precluding the internal modifications of pre-existing 3D structures, without affecting the integrity of the structures of interest.

On the other hand, injectable materials used as delivery vehicles hold great promise to improve the therapeutic efficacy for functional recovery of diseased or injured tissues and organs, including stem cell-based therapies¹³. An injectable hydrogel is the preferred material form for stem cell transplantation due to its potential to mimic the native stem cell microenvironment¹⁴⁻¹⁶. A variety of crosslinking strategies have been developed to form hydrogel structures in internal regions of tissues: *i*) physical crosslinking, which include ionic crosslinking and stimuli-responsive crosslinking (such as temperature and pH change); *ii*) chemical crosslinking, which includes enzymatic, radical or click chemistry, and provides better control of the hydrogel mechanical strength and degradation, compared to physical crosslinking processes¹³. However, independently from the crosslinking strategy used, injectable hydrogels form an isotropic structure around the site of the injection which cannot be controlled in terms of 3D shape and spatial organization.

In this work, we envision the possibility to inject photo-active polymers in living animals and to directly fabricate *in situ* spatially-controlled 3D constructs across and within tissues. To date, this concept, that we name intravital 3D bioprinting (i3D bioprinting), has never been reported.

Compared to conventional 3D bioprinting, i3D bioprinting should confront and surpass additional hurdles, which are intrinsic to *in vivo* application. These include *i*) fabrication across tissues without inducing tissue damage or interfering with the pre-existing 3D tissue anatomical structures; *ii*) fabrication efficiency should not be affected by physiological tissue displacements given by heart beating as well as breathing of the live animals; *iii*) accurate (XYZ) positioning and orientation of 3D bioprinted structures within tissues at site of interest to support cell function and/or tissue regeneration. Ideally, 3D bioprinting in a live animal would also require accurate pre-processing imaging for fine 3D mapping the anatomical area in which the printed object needs to

Deleted: minimally invasive

Deleted: (minimal invasiveness)

be manufactured, and post-processing analysis to effectively evaluate the positioning, the orientation and the accuracy of the printed object.

We challenged these hurdles by developing photosensitive biopolymers that can be used to fabricate hydrogels within and across solid matrices or tissues. These biopolymers can be crosslinked *in vitro* in presence of living cells or inside a pre-mixed gels for controlling organoid shape and behavior in a 3D culture. Moreover, after a simple injection inside the desired anatomical site (i.e. within tissues), photosensitive biopolymers can be photo-crosslinked *in vivo* to form a 3D object by using near-infrared (IR) laser light associated with high-spatial resolution intravital multi-photon microscopy specifically designed for 3D object fabrication (**Fig. 1**, named i3D bioprinting). This was accomplished by modifying biocompatible hydrophilic polymeric backbones with a hydrophobic photo-active crosslinking group, which efficiently undergoes cycloaddition when two-photon (2P) excited at wavelengths longer than 850 nm. In virtue of the selected wavelength range, femtosecond IR tightly-focused pulsed laser light can penetrate through soft tissues¹⁷, allowing 3D hydrogel photo-crosslinking inside tissues and across tissues. We showed that complex 3D hydrogels of branched polyethylene glycol (PEG) and gelatin (Gel) are accurately fabricated into tissues of living mice such as dermis across epidermis, skeletal muscle across epimysium or brain across meninges. The 3D hydrogels show high biocompatibility and incorporation of functional vascular network, which makes the i3D bioprinting a procedure suitable for clinical translation. Finally, we show that i3D bioprinting allows spatially-controlled donor cell grafting and, importantly, supports the generation of newly formed myofiber bundles integrated with host functional vascular network.

Development of IR photo-crosslinking strategy.

We initially developed a technology to enable photo-crosslinking of biopolymers into hydrogels by using laser wavelengths that allow deep tissue penetration¹⁷ ($\lambda > 800$ nm). Accordingly, we selected coumarin derivatives as photo-sensitive crosslinking moieties for the end functionalization of polymeric backbones. Coumarin derivatives have the potential to undergo [2+2] cycloaddition when exposed to single photon UV-Vis light^{18–20} or under 2P excitation at near-IR light^{18,21,22}. UV-Vis light photo-crosslinking can be performed to fabricate hydrogels in which coumarin derivatives have been used as photo-sensitive crosslinking moieties^{23–26}. However, UV-Vis wavelengths are incompatible with tissue penetration¹⁷. Few applications reported the use of coumarin-derivatives for 2P hydrogel degradation^{25,26}, but not for 2P hydrogel fabrication. On the other hand, coumarin-derivatives were initially developed as fluorescent dyes, so that *in vivo* imaging of 3D coumarin-based hydrogel structures and their accurate positioning and orientation within living animals will be facilitated. Finally, coumarin-mediated cycloaddition offer the additional advantage of avoiding possible toxicity for living tissues, based on their radical- and photo-initiator-free chemistry²⁷.

We considered 58 known coumarin derivatives (**Suppl. Tab. S1**), and 8 of them were selected for further characterization based on ring substituents that can impact their light-absorption properties and the chemistry for backbone conjugation (**Fig. 2a**, **Extended Data Fig. 1** and **Suppl. Tab. S2**). Among them, 7-hydroxycoumarin-3-carboxylic acid (HCCA) was defined as an optimal candidate for i3D bioprinting application because it has an electron-donating substituent in the 7-position and an electron-withdrawing substituent in the 3-position, which promote a red-shift of the maximum absorption peak thus offering an advantage in term of tissue permeability to laser light (**Extended Data Fig. 1,2**). Moreover, the presence of a carboxylic group allows the conjugation

Deleted: minimally invasive

Deleted: ,

of HCCA to polymers, such as linear PEG, branched PEG, and gelatin (Gel) (**Fig. 2b** and **Extended Data Fig. 3,4**) which are among the most common and better characterized polymers used to fabricate biocompatible hydrogels³⁻⁵. HCC-PEG conjugates were characterized by ¹H-NMR and Fourier transform infrared (FT-IR) analysis, and size-exclusion chromatography (SEC) demonstrated HCC-Gel conjugation (**Extended Data Fig. 5-7**). The conjugation degree was also quantified, and absorbance spectra were analyzed for all the HCC-polymers (**Extended Data Fig. 8**).

To test light-mediated cycloaddition of HCC-polymers, we initially used HCC-conjugated linear PEG (HCC-PEG) as model. Single-photon excitation ($\lambda = 365$ nm) was able to induce HCC-PEG intermolecular cycloaddition in solution, resulting in dimerization of HCC-PEG as showed by spectrophotometric analysis (**Fig. 2c**). The ability of HCCA to undergo cycloaddition was further confirmed by ¹H-NMR spectroscopy and electrospray ionization mass spectrometry analysis of HCCA solution (**Extended Data Fig. 9,10**). Moreover, HCC underwent cycloaddition after 2P excitation at a wavelength of 850 nm using a multi-photon laser-scanning microscope, as showed by the rapid 2D HCC-PEG patterning (~ 10 sec per $850 \mu\text{m}^2$) onto HCCA-functionalized glass slides with high spatial precision (**Fig. 2d**).

2P Hydrogel fabrication.

We then tested the possibility of assembling 3D hydrogel constructs by using branched PEG and Gel polymers conjugated to HCCA and excited in a wide wavelength window. In order to screen for wavelengths ($700 \text{ nm} < \lambda < 1000 \text{ nm}$) that allow 2P crosslinking at mild laser power (0.7 mW), we found that hydrogels made of HCC-4arm PEG, HCC-8arm PEG and HCC-Gel remain in shape after removal of the solution containing non-crosslinked polymers when fabricated at $700 \text{ nm} < \lambda < 850 \text{ nm}$ (**Extended Data Fig. 11**). By increasing laser power up to 2 mW, HCC-8arm PEG and HCC-Gel can be crosslinked up to 900 nm (data not shown). Crosslinking is triggered only within the focal region (voxel) and the laser-scanning path of the multi-photon microscope provides spatial control of the reaction. Typically, Z-stacks of regions of interest were 2P excited. Based on the optical properties of the objective used, a Z-spacing of $1 \mu\text{m}$ between adjacent planes was used. Thus, 3D structures with complex morphology could be easily fabricated by sequential addition of Z-stacks of multiple regions of interest (**Fig. 2e** and **Extended Data Fig. 12**), including a readable barcode (**Extended Data Fig. 12c**), words (**Extended Data Fig. 12c-d** and **Suppl. Video S1**) or a hollow cube (**Extended Data Fig. 12e** and **Suppl. Video S2**). Figure 2e shows parallelepipeds that are 45° rotated on the same Z plane to form an asterisk.

Accuracy of 3D photo-crosslinking was further confirmed after fabrication of hydrogels by photo-crosslinking multiple Z positions, (**Fig. 3a**) or by assembling additively multiple parallel linear objects. The minimal linewidth ($1.9 \pm 0.2 \mu\text{m}$) of fabricated linear objects (**Fig. 3b**) and the sub-micrometric resolution of the bioprinting (**Fig. 3c**) was achieved. Accordingly, a 3D single line flower-shaped hydrogel of HCC-Gel was fabricated using a computer drawing pad combined to a free line scan program of the multi-photon microscope (**Fig. 3d** and **Suppl. Video S3**). Additionally, we tested the maximum 3D object dimension ($\Delta Z \sim 2 \text{ mm}$) that was possible to fabricate without changing printing parameters (scanning speed and laser power; **Fig. 3e** and **Suppl. Video S4**).

Considering the final *in vivo* application and taking in account the displacement due to animal respiratory movements and pulsed blood flow, we quantified an optimal writing time per single line (ms/line), which allows 3D hydrogel production with structural integrity (**Fig. 3f**). The optimal writing time of 1 ms/line was therefore used for the i3D bioprinting experiments; lower levels of

Formatted: Font: Not Bold

laser powers does not trigger 2P-crosslinking, whereas higher powers may induce heat damage. This efficient and fast bioprinting, able to preserve minimum feature dimension, is likely due to the threshold behavior and nonlinear nature of multi-photon excitation¹⁷ combined with highly efficient cycloaddition. In conventional 2P polymerized hydrogels, a photo-initiator and possible co-initiator or sensitizer molecules activate a free radical chemical crosslinking reaction through a diffusion-reaction mechanism^{28,29}. In the case of coumarin-conjugated dipeptides (7-(diethylamino)-3-coumarin carboxylic acid), it was previously reported that cycloaddition is facilitated when coumarin moieties are in close proximity^{23,24}. Others showed that coumarin-based polymers generate micelles in aqueous solution¹⁸. In line with this, we observed by transmission electron microscopy (TEM) imaging that HCC-PEG forms nano-assemblies (**Extended Data Fig. 13**), supporting the idea that HCC-polymer in aqueous solution can self-assemble into supramolecular structures, in which the HCC photo-active groups are brought in close proximity and are ready to undergo fast cycloaddition upon light excitation, resulting in efficient crosslinking reactions within a focused 2P optical voxel.

Over the last decade several reports have highlighted the paramount role of stiffness in regulation of cell behavior^{30,31}. Atomic force microscopy has been used to estimate the hydrogel elastic properties³², which are strictly correlated with the hydrogel photo-crosslinking rate³³. Interestingly, we were able to finely tune the stiffness of HCC-4arm PEG or HCC-Gel hydrogels over biological-matched ranges (1 kPa – 20 kPa) by modulating the laser power (**Fig. 3g**). Indeed, multi-photon microscopes allow fine tuning of laser power³⁴, which in turn can modulate hydrogel photo-crosslinking rate³³, the crosslinking density and, consequently, the hydrogel mechanical properties³².

To better characterize hydrogel photo-crosslinking rate on multiple samples and larger volume in conventional fabrication conditions, 7-Carboxymethoxy-4-methylcoumarin (CMMC)-4arm PEG and CMMC-Gel were specifically designed and produced to perform 1-photon UV mediated cycloaddition (**Fig. 2a** and **Extended Data Fig. 14,15**). The elastic modulus increases to asymptotic values by increasing the irradiation time, showing a sigmoidal temporal profile of elastic modulus that reached the polymer crosslinking saturation, independently from the polymeric backbone used (**Fig. 3h**). Interestingly, the modulation of elastic modulus of hydrogels obtained with 1P and 2P photo-crosslinking (with CMMC-Gel and HCC-gel, respectively) by varying the polymer concentration showed remarkable similarity (**Fig. 3i**).

Altogether these results demonstrated the ability to fabricate 3D hydrogels with precise XYZ positioning, micrometric resolution and tunable physiological stiffness by using IR light-mediated photo-crosslinking of HCC-polymeric solutions.

In vitro biocompatibility.

Given that hydrogels need to be fully biocompatible, we firstly assessed the ability of HCC-Gel to support *in vitro* culture of different cell types. Pre-assembled flat HCC-Gel hydrogels ($\Delta Z = 30 \mu\text{m}$) supported adhesion and culture of HUVEC cells (**Extended Data Fig. 16a**) and human embryonic stem cell-derived neural stem cells (hES-derived NSCs; **Fig. 4a** and **Extended Data Fig. 16b-d**). Three days after seeding, hES-derived NSCs showed expression of specific neural markers and absence of apoptosis when cultured on pre-assembled flat HCC-Gel hydrogels (**Fig. 4a** and **Extended Data Fig. 16e**). Fibroblasts (FBs) derived from green fluorescent protein (GFP)-expressing mice efficiently adhere to parallelepiped-shaped HCC-Gel hydrogels characterized by

different size (ΔZ up to 150 μm) and interspace (down to 10 μm) and change their morphology according to the 3D shape of fabricated hydrogels (**Extended Data Fig. 17**).

We further confirmed the biocompatibility of HCC-Gel solution and of the photo-crosslinking strategy by using cell-laden HCC-Gel solution. Six hours after hydrogel crosslinking, FBs were viable and embedded within 3D hydrogel structures (**Fig. 4b**, **Extended Data Fig. 18** and **Suppl. Video S5**). Interestingly, the elastic modulus of bioprinted structures was not strongly changed by the presence of cells (Young's modulus was reduced by about 6% in presence of cells, **Fig. 4c**), suggesting that the 2P-crosslinking and hydrogel fabrication were not substantially affected by cells suspended in the HCC-Gel solution. Then, we evaluated cell viability comparing cell-laden constructs obtained with conventional single photon hydrogel crosslinking ($\lambda = 365$ nm, single photon, CMMC-Gel)^{28,29}, those fabricated with 2P bioprinting ($\lambda = 850$ nm, 2-photon, HCC-Gel), compared to irradiated-only ($\lambda = 365$ nm, Matrigel) or unirradiated (Matrigel) controls. Two days after 3D culture, cell viability was between 90-99% in all conditions (**Fig. 4d**). We noticed that with our set-up single photon irradiation time up to 3 minutes and 2P bioprinting laser power up to 1 mW give good cell viability (as used in **Fig. 4d**), whereas increasing laser power was detrimental for viability (data not shown).

In vitro cell instructive hydrogel.

Starting from these results, we then asked whether the shape of 3D bioprinted cell-laden HCC-Gel could provide specific topological cues. To investigate this, we used the ability of murine muscle-derived stem cells (MuSC) to differentiate into myotubes and to adapt their morphology and orientation based on microenvironment topology^{35,36}. As confirmed by quantification of cell directionality, single-nucleated or polynucleated cells within elongated-shaped HCC-Gel structures appeared oriented along major axis of the 3D structures (**Fig. 4e**, left panel; **Fig. 4f**), whereas cells located in cuboid-shaped HCC-Gel structures were randomly oriented (**Fig. 4e**, right panel; **Fig. 4f**).

Finally, to evaluate whether HCC-Gel hydrogels were able to support cell culture for longer time and cell functionality, MuSCs were cultured on parallelepiped-shaped HCC-Gel structures for 10 days. Microscopic analysis demonstrated that parallelepiped-shaped HCC-Gel hydrogels support the formation of aligned multinucleated myotubes (**Fig. 4g**) that showed spontaneous contraction 5 days after induction of cell differentiation (**Suppl. Video S6**).

These data demonstrated that the photo-crosslinking of HCC-Gel does not affect cell viability, is compatible with cell-laden 3D bioprinting, and supports stem cell differentiation and cellular function. It is worth underlining that our setup can be also employed synergistically to conventional 3D bioprinting strategies⁵.

In vitro bioprinting into pre-existing human organoid 3D culture.

i3D bioprinting entails additional complexities: 3D bioprinting needs to be performed into anatomical sites of living animals, such as tissues, body cavities or extracellular matrix that may include a variety of components of the interstitial space. Thus, we then tested the possibility of fabricating 3D hydrogel objects into a pre-existing 3D matrix. For this purpose, we used Matrigel, a gel formed by a basement membrane equivalent widely used for 3D cultures of cells and organoids. 50/50 HCC-Gel/Matrigel mixture (v/v) was used to crosslink HCC-Gel 3D structures of defined XYZ position and orientation within the gel. HCC-Gel 2P photo-crosslinking showed a bio-orthogonal reaction in pre-existing gel (**Fig. 5a**, and **Suppl. Video S7**). When fabricated into pre-existing 3D Matrigel, hydrogel structures remained in shape also after Matrigel dissociation

Formatted: Font: Not Bold

and, interestingly, showed comparable elastic modulus of hydrogel fabricated in absence of Matrigel (**Fig. 5b**). Furthermore, HCC-Gel/Matrigel 3D gels were able to support the viability and the growth of human small intestinal organoids (hSIOs, **Extended Data Fig. 19**), which is a challenging *in vitro* 3D human culture³⁷, while preserving the possibility of fabricating crosslinked objects within the gel. With this in mind, we fabricated 3D parallelepipeds accurately positioned and oriented relative to selected hSIOs within the 3D gel culture (**Fig. 5c**, **Extended data Fig. 20** and **Suppl. Video S8**). Further analysis of such culture can also be performed, as shown by the intestinal epithelial marker, Ezrin, and f-actin staining (**Extended data Fig. 20b**). HCC-Gel hydrogel cytocompatibility on hSIOs enclosed in the structures was demonstrated by live/dead assay performed after 2 days and 8 days of culture (**Fig. 5d** and **Extended Data Fig. 21a**).

Then, we investigated whether bioprinted HCC-Gel walls within Matrigel and specifically positioned around individual hSIOs could affect their biological behavior (**Fig. 5c**). hSIOs confined inside an open square-box (formed by 4 orthogonal walls) grew normally and after few days of culture touched and deformed HCC-Gel hydrogel walls (**Fig. 5e** and **Extended Data Fig. 21b**). Between day 6 and day 8 of culture, hSIOs enclosed in HCC-Gel-based hydrogel showed marked morphology changes, which lead to well-developed columnar epithelium (**Fig. 5f**). This morphology was characterized by thickening of the organoid wall, F-actin localization in apical position and nuclei constriction in the basal domain as quantified by the basal-apical distance ratio and the basal/apical axis (**Fig. 5g-i**). In comparison, hSIOs cultured in the same hydrogel composition but without any contact with HCC-Gel structures did not show such morphological changes (**Fig. 5f**).

Interestingly, the basal localization of beta4-integrin observed in hSIOs enclosed in HCC-Gel structures (**Fig. 5i**) suggests that cell adhesion could be one possible mechanism involved in the observed phenotype. To dissect the contributions of extrinsic mechanical *vs* biochemical signals in triggering the organoid morphological changes, hSIOs cultured in Matrigel were enclosed inside an open square-box made of HCC-8arm PEG-based hydrogel, which is well-known to display cell repellent properties^{8,38,39}. We prove that HCC-8arm PEG/Matrigel allowed hSIO survival and growth in culture (**Fig. 5j**). However, differently from what observed with HCC-Gel, hSIOs enclosed in HCC-8arm PEG-based hydrogel did not show columnar epithelium after 8 days of culture, hydrogel deformation, actin apical localization nor nuclei constriction (**Fig. 5k,l**). Instead, hSIOs morphology reflects the 3D shape of the enclosed open-box made by HCC-8arm PEG-based hydrogel. As confirmed by Feret's angle quantification, only hSIOs enclosed by HCC-8arm PEG acquired a cuboidal cystic structure 6 days after culture, when compared to HCC-Gel enclosed hSIOs (**Fig. 5m**).

It has been shown that mechanical properties of synthetic hydrogel have a role in expansion and differentiation of murine SIOs⁴⁰, whereas the effect of hydrogel stiffness on hSIO behavior remains unclear. Our results suggest that the formation of columnar epithelium of hSIO could be correlated to the hydrogel biochemical composition rather than its pure mechanical properties, since HCC-Gel and HCC-PEG were fabricated for having the same Young's modulus. It would be of future interest to use this approach to investigate the cues that give rise to columnar epithelium in hSIOs.

In vivo hydrogel bioprinting.

Our next goal was to test whether i3D printing is possible across tissues and inside tissues. Skin was identified as an optimal target organ to perform i3D printing without open surgery. The HCC-polymer solution was locally delivered *in vivo* by intra-dermal injection in wild-type or GFP+

transgenic mice. Then, the HCC-polymer solution was exposed to focalized pulsed near-IR laser light ($\lambda = 850$ nm) using a 2P microscope (**Fig. 6a**). Either wild-type or GFP⁺ transgenic mice were anesthetized and subjected to i3D bioprinting in the skin. With this setup, we succeeded in efficiently fabricating isolated 3D objects inside the dermis of living animals (**Fig. 6b** and **Extended Data Fig. 22a**). In GFP⁺ mice, by taking advantage of fluorescence imaging of host tissues, we could easily visualize both the manufactured objects located inside dermis, and the integrity of the epidermis above the crosslinked hydrogel (**Fig. 6b** and **Suppl. Video S9**). The exact localization could be revealed by the hair bulb position (**Fig. 6b**, arrow). The high compatibility of i3D bioprinting was further confirmed by the integrity of the skin after the entire procedure, which was comparable to untreated tissue (**Fig. 6b,c**). Furthermore, as demonstrated *in vitro*, we showed that i3D bioprinting across epidermis allows the manufacture of 3D hydrogel structures with micrometric linewidth (**Extended Data Fig. 22b**), and the fabrication of inserts with a variety of morphologies thanks to the precise XYZ positioning (**Extended Data Fig. 22a**).

Once demonstrated that i3D printing can be performed across epidermis without open surgery, we tested if such technology was applicable to other tissues. Thus, a minimal surgical procedure was applied to expose intact skeletal muscle or brain and HCC-polymer solutions were injected below the epimysium or meninges, respectively, and above the tissues of interest. Photosensitive solutions injected under the epimysium of skeletal muscle were photo-crosslinked to fabricate 3D hydrogels at the surface of muscle fibers without evident alteration of the overall muscle fiber morphology and connective tissue integrity (**Fig. 6d,e**, **Extended Data Fig. 23** and **Suppl. Video S10,S11**). 2P-crosslinked hydrogels were formed only in the area where the reaction was performed (**Fig. 6f**). Our experimental setup allows real-time imaging during and after i3D bioprinting, giving the possibility of triggering hydrogel crosslinking in a specific anatomical site, i.e. a single myofibre *versus* a bundle of myofibers. Given the natural anatomic patterning of myofibres, skeletal muscle was also used to verify the ability to fabricate i3D bioprinted hydrogels by precisely tuning their XYZ position and orientation. Multiple objects were fabricated in a parallel or orthogonal fashion when compared to their position and/or to myofiber orientation (**Extended Data Fig. 24**). The versatility of the fabrication protocol was further proved by performing i3D bioprinting of a HCC-Gel hydrogel displaying infinite-symbol shape, using the design realized with a computer drawing pad as input for the free line scan program of the multi-photon microscope (**Extended Data Fig. 25**).

Safe i3D bioprinting was also possible in a particularly vulnerable tissue such as brain. Burr hole was performed into the skull of mice to allow HCC-polymeric solution injection across meninges, and subsequent hydrogel crosslinking was achieved by using 2P excitation through multi-photon microscope (**Fig. 6g**). Importantly, we found absence of bleeding foci and a correct maintenance of blood flow at the area of i3D bioprinting in the brain (**Fig 6g** and **Extended Data Fig. 26a**). 2P crosslinked hydrogels surrounded and embedded the host vasculature network without damaging the vessels and preserved blood flow, as shown by red-dextran tracing (**Fig. 6h** and **Extended Data Fig. 26b**). These results further confirmed the biocompatibility of i3D bioprinting.

In vivo biocompatibility.

To reach the above results and effectively translate 3D hydrogel fabrication *in vivo*, we optimized laser power and writing time across tissues balancing crosslinking efficiency, velocity of 3D bioprinting (to reduce the effect of movements associated to breathing and cardiac beating), and heat-induced tissue damage. The optimal writing time (1 ms/line) was combined with the optimal laser power (1 mW) to obtain a stable hydrogel under epimysium without myofiber damage, as the

Formatted: Font: Not Bold

Formatted: Font: Not Bold

Formatted: Font: Not Bold

appearance of heat-induced damage, myofiber contraction and cleavage of cell death-marker caspase-8^{41,42} were absent (**Extended Data Fig. 27**). Myofiber damage was observed only after 2P irradiation with 3-fold increased laser power and ~17-fold increased time of irradiation per single confocal plane, when compared to i3D bioprinting condition (**Extended Data Fig. 27**).

5 Therefore, we investigated the biocompatibility of HCC-4arm PEG and HCC-Gel solution. HCC-4arm PEG crosslinked hydrogels were found to be preserved *in vivo* 4 days after i3D printing across epimysium, with no evident tissue damage at the site of 2P-crosslinking as shown by imaging analysis (**Extended Data Fig. 28a, b**). Consistent with PEG biocompatibility studies⁴³, immunofluorescence analysis showed recruitment of macrophages to the site of hydrogel crosslinking, despite the fact no evident histological changes were observed (**Extended Data Fig. 28c, d**). Since PEG hydrogels are cell repellent^{8,38,39}, and based on previous *in vitro* results, we further investigated *in vivo* biocompatibility of our injectable HCC-Gel hydrogels before challenging longer term i3D printing in the presence of donor cells (i3D bioprinting). In order to prove biocompatibility of HCC-Gel, the polymeric solution was subcutaneously injected into wild type mice and histological (Haematoxylin-eosin and Masson trichromic) staining, TUNEL test, and immunofluorescence staining for macrophages were performed after 4, 7 and 21 days. When compared to animals treated with PBS, no evident histological modification, cell apoptosis or macrophage infiltration were observed (**Extended Data Fig. 29**).

20 Lastly, we aimed at showing that i3D bioprinting could be effectively employed in live animals for *i*) delivering cells in a spatially controlled manner; *ii*) allowing precise cell grafting into a defined anatomical site; and *iii*) supporting a proper structural organization of *de novo* tissues.

In vivo spatially controlled cell engraftment.

25 We then investigated if i3D bioprinting could instruct spatial control of cell engraftment by firstly employing HCC-Gel laden with primary mCherry⁺FBs, delivered across the epimysium of murine hind limb of isogenic immunocompetent animals. Distinct freshly fabricated HCC-Gel structures containing embedded mCherry⁺FBs were located between the epimysium and skeletal muscle of host wild-type mice accordingly with the bioprinted structures (**Extended Data Fig. 30a**). Then, longer term studies were performed for investigating the effect of cell-laden i3D bioprinting on donor cells. The mCherry⁺FBs suspended into HCC-Gel solution were injected under the epimysium (no i3D bioprinting) or injected and subjected to i3D bioprinting for the generation of parallelepiped-shaped constructs. Donor mCherry⁺FBs were identified in host animals 21 days after delivery in both experimental conditions (**Extended Data Fig. 30b-h**). However, imaging analysis showed elongated clusters of mCherry⁺FBs only in i3D bioprinted animals, which followed the posteroanterior axis of the parallelepiped-shaped constructs defined during i3D bioprinting (**Extended Data Fig. 30b-e**). Conversely, injected cells that did not undergo i3D bioprinting were organized into rounded clusters (**Extended Data Fig. 30b, f-h**). To extend these results to another tissue, i3D bioprinting was also performed across the epidermis. Elongated localization of mCherry⁺FBs was observed 14 days after intra-dermal injection and i3D bioprinting of embedded donor cells into parallelepiped-shaped constructs, when compared to mCherry⁺FBs injected only, that conversely remained localized into rounded clusters (**Extended Data Fig. 30i**). These data strongly suggested that i3D bioprinting can elicit a desired spatial organization of delivered cells.

Intravital bioprinting for de novo tissue formation.

Formatted: Font: Not Bold

Finally, we aimed at demonstrating that i3D bioprinting has the potential to support *de novo* tissue formation. As a tissue model, we used skeletal muscle since its formation requires anisotropic cell alignment during the early stages of skeletal muscle regeneration⁴⁴⁻⁴⁶.

Numerous stem cells have been shown to possess myogenic potential and thus have been applied for cell therapy-based regenerative medicine approaches aimed at promoting skeletal muscle regeneration⁴⁵. In particular, MuSCs can give rise to a large number of progeny able to contribute extensively to the formation of new muscle fibers when transplanted *in vivo*⁴⁴⁻⁴⁶. Moreover, MuSCs show the ability to regenerate skeletal muscle when *in situ* embedded into a photo-crosslinked hydrogel to repair a volumetric muscle loss damage⁴⁷. However, the proper differentiation of MuSCs and maturation of myotubes into aligned myofibers follow restricted 3D spatially defined patterns^{35,36}. Since FBs have been shown to support and sustain skeletal muscle regeneration⁴⁸⁻⁵⁰, we designed an experimental strategy in which HCC-Gel solution laden with both FBs and MuSCs was employed for testing whether i3D bioprinting of parallelepipeds could promote *de novo* skeletal muscle formation. A defined ratio⁵¹ of GFP⁺MuSCs to mCherry⁺ in HCC-Gel solution were injected and then i3D bioprinted into multiple parallelepiped-shaped constructs (Fig. 7a). As controls, animals were also injected with cells resuspended in PBS, in Matrigel or HCC-Gel solution without 2P irradiation (Fig. 7a and Extended Data Fig. 31a-c). One week after treatments, confined bundle of elongated GFP⁺ cells was observed only in animals that underwent i3D bioprinting (Fig. 7a,b). Conversely, after injection without i3D bioprinting, sparse cells were found in the host tissue (Fig. 7b and Extended Data Fig. 31a-c). In agreement with previous results, quantification of cell directionality showed that i3D bioprinting allows the generation of a spatially controlled cell engraftment (Fig. 7c). Remarkably, the bundle of elongated GFP⁺ cells were integrated by the host tissue, with a functional three-dimensionally organized vascular network observed only in i3D bioprinted animals (Fig. 7b). Immunofluorescence analysis confirmed that *de novo* formed tissue is constitute of regenerating myofibers as confirmed by the expression of embryonic myosin heavy chain protein (eMHC), which is a marker of newly formed myofibers (Fig. 7d). Striated organization of the muscular cytoskeleton, as well as presence of branched and centrally nucleated myofibers were also observed (Fig. 7e) and mCherry⁺FBs were founded at the periphery of GFP⁺ myofibers derived from donor GFP⁺MuSCs (Extended Data Fig. 31d). Immunostaining for GFP, laminin and nuclei was used to quantify centrally nucleated myofibers. The analysis revealed that donor myofibers are mostly centrally nucleated, conversely host myofibers do not show centrally located nuclei, indicating that muscle regeneration is restricted to donor-derived tissue (Fig. 7f). Altogether, these results indicate that i3D bioprinting supports *de novo* skeletal muscle tissue formation, which was characterized by proper structural organization and integration with the host vascular system.

In summary, we show that i3D bioprinting allows the fabrication of hydrogels that can support the maintenance of cell functionality and can be used to modulate their behavior. With this approach, bioprinting is possible not only *in vitro* into pre-existing 3D environments (Matrigel), but also across tissues in different target organs in live animals together with real-time imaging.

By allowing hydrogel fabrication into pre-existing 3D environments, i3D bioprinting technology represents an innovative strategy that could be used to advance our understanding of *in vitro* organoid models. Deliberate regulation of self-organization and morphogenesis hold the potential to ameliorate organoid topology and reproducibility, as well as to dissect mechanotransduction and biochemical mechanisms underpinning specific cell responses in 3D culture conditions⁵². Furthermore, i3D bioprinting is envisioned as a mean to perform *in vivo* 3D confined cell delivery,

- Deleted: a
- Deleted: elongated
- Deleted: were
- Formatted: Font: Not Bold
- Deleted: 31a
- Moved (insertion) [1]
- Deleted: i
- Deleted: f
- Deleted: Histological analyses of muscle sections showed the presence of centrally nucleated myofibers longitudinally located on the periphery of the underlying host muscle and surrounded by connective tissue (Extended Data Fig. 31b).
- Formatted: Font: Italic
- Deleted: expressing
- Deleted: also revealed s
- Formatted: Font: Bold
- Deleted: d-
- Deleted:).
- Deleted: confirmed the presence of
- Deleted: Moreover,
- Deleted: donor cells, with
- Formatted: Font: Bold
- Deleted: c,d
- Formatted: Font: Not Bold
- Deleted: Expression of the embryonic isoform of myosin heavy chain together with the presence of centrally located nuclei further demonstrated that GFP⁺ myofibers were newly generated (Fig. 7e-e). Finally, and
- Formatted: Font: Not Bold
- Moved up [1]: in agreement with previous results, quantification of cell directionality showed that i3D bioprinting allows the generation of a spatially controlled cell engraftment (Fig. 7f).

capable of instructing cell structural organization within tissues. This represents a novel strategy to improve engraftment of cells after injection within tissues, avoiding fast dispersion and the short life-time of cells that typically occurs with this delivery strategy⁵³.

5 The i3D technology offers an unprecedented opportunity to study cell biology and physiology in 3D environments, where the internal structure and organization can be modified according to the biological needs both *in vitro* and *in vivo*. It is worth to underline that this approach could suffer from limitations related to the multi-photon microscopy, such as the size and depth of hydrogel crosslinking that falls into millimeter scale. Conversely, research in multi-photon microscopy/lithography is rapidly developing novel strategies to overcome such limitations⁵⁴, including deep tissue penetration with 3 photon excitation⁵⁵, optical fiber guidance⁵⁶ and multi-photon holographic technology^{57,58}. At the current stage, i3D bioprinting is limited to tissues that are accessible to the light source. However, we envision that in the future i3D bioprinting can benefit from the above developing strategies and can be coupled with emerging optical imaging-guided surgery^{59,60}, opening new paradigm in minimally invasive-surgical techniques suitable for organ repair, reconstruction and *de novo* fabrication.

10

15

Deleted: We envision that in the future,

Deleted: such

Methods:

Chemicals

Two kDa methoxy PEG amine (mPEG-NH₂), 10 kDa 4-arm PEG amine pentaerythritol core (4arm-PEG-NH₂), 20 kDa 8-arm PEG amine tripentaerythritol core (8arm-PEG-NH₂) were obtained from Jenkem Technology (Allen, TX, USA). 7-hydroxycoumarin-3-carboxylic acid (HCCA) and ethyl 7-hydroxycoumarin-3-carboxylic acid (HCCA) were purchased from TCI Chemicals (Tokyo, Japan). Gelatin from porcine skin (Gel, type A, 300 bloom, cell culture tested), 7-(carboxymethoxy)-4-methylcoumarin (CMMC), 7-hydroxycoumarin (HC), 7-hydroxy-4-methylcoumarin (HMC), 7-hydroxy-4-(trifluoromethyl)coumarin (HTMC), 7-amino-4-methyl-3-coumarinylacetic acid (AMCAA), N-hydroxysuccinimide (NHS), N,N'-dicyclohexylcarbodiimide (DCC), triethylamine (TEA), 2,4,6-trinitrobenzenesulfonic acid (TNBS), 3-aminopropyltriethoxysilane (APTES), Dulbecco's Phosphate Buffered Saline without calcium and magnesium chloride (PBS), anhydrous dimethylsulfoxide (DMSO), diethyl ether, absolute ethanol, deuterated chloroform (CDCl₃), deuterated DMSO (DMSO-d₆), acetonitrile and trifluoroacetic acid were purchased from Sigma-Aldrich (St. Louis MO, USA). Water for the preparation of all solutions was "ultrapure" water (Milli-Q, 0.06 μSiemens cm⁻¹) produced with a Millipore Milli-Q purification system (MA, USA). Salts and buffers were purchased from Fluka Analytical (Buchs SG, Switzerland) and Sigma-Aldrich (St. Louis, MO, USA).

Microscopes used for imaging

For intravital imaging, i3D bioprinting and *in vitro* imaging, Scientifica 2-photon microscope, equipped with a Nikon LWD 16x/0.80 W DIC N2 WD3.0 objective, and with a pulsed Ti:Sapphire laser (Chameleon Vision II, Coherent) of 140 fs pulse width at peak, and 80 MHz repetition rate was used. Confocal microscopes Leica TCS SP5 or Zeiss LSM710 were used for confocal image acquisition. Epifluorescence microscopes Leica DMIL LED or Olympus BX60 equipped with Olympus DP50 digital camera were used for *in vitro* imaging. Fluorescence stereomicroscope Leica MZ16F equipped with Canon EOS1000D camera were used to perform in brain hydrogel injection and imaging after i3D bioprinting.

Animals

All the procedures performed on animals were approved by the Ethics Committee of the University of Padova and authorized by the Italian Ministry of Health, animal license n. 601/2017-PR. We performed experiments in 4-6 month old wild-type mice of both female and male inbred C57BL/6J strain and in transgenic C57BL/6-(ACTB-EGFP)/J mice. Mice were housed in individual cages in an environmentally controlled room (23 °C, 12 h light/12 h dark cycle) and provided food and water ad libitum. For *in vivo* studies, the number of animals used ranged from 4 to 6 per each experimental condition.

Analysis of absorbance spectra of coumarin derivatives

Selected coumarin derivatives were dissolved in DMSO at a concentration of 5 mg/mL and diluted to 10 μg/mL in PBS, pH 7.4. The absorption spectra were recorded using an Evolution 201 UV-Vis spectrophotometer (Thermo Fisher Scientific, Waltham, MA, USA) in the wavelength range of 250-450 nm.

Synthesis of linear HCC-PEG, HCC-4arm PEG and HCC-8arm PEG

HCCA (1.00 g, 4.85 mmol) was dissolved in anhydrous DMSO (20 mL), then NHS (1.12 g, 9.70 mmol) and DCC (2.00 g, 9.70 mmol) were added to the solution. The reaction mixture was stirred overnight in the dark and filtered to remove the insoluble dicyclohexylurea. The 7-hydroxycoumarin-3-carboxylic acid N-succinimidyl ester (HCCA-NHS) was isolated by precipitation in diethyl ether (450 mL). HCCA-NHS was washed with diethyl ether (30 mL × 3) and finally desiccated under vacuum.

mPEG-NH₂ (1.00 g, 0.50 mmol) was dissolved in anhydrous DMSO (10 mL), then triethylamine (69.69 μL, 0.50 mmol) and HCCA-NHS (0.30 g, 1.00 mmol) were added to the solution. 4arm-PEG-NH₂ (1.00 g, 0.10 mmol) was dissolved in anhydrous DMSO (10 mL) and added of triethylamine (55.75 μL, 0.40 mmol) and HCCA-NHS (0.24 g, 0.80 mmol). 8arm-PEG-NH₂ (1.00 g, 0.05 mmol) was dissolved in anhydrous DMSO (10 mL) and added of triethylamine (55.75 μL, 0.40 mmol) and HCCA-NHS (0.42 g, 1.40 mmol). After 12 h of stirring at room temperature in the dark, the reaction mixtures were added dropwise to diethyl ether (300 mL). The precipitates were recovered by centrifugation at 1950 × g and dried under vacuum. The crude products were dissolved in a 9:1 (v/v) Milli-Q water/DMSO mixture and dialysed using Spectra/Por dialysis membranes (SpectrumLabs, Rancho Dominguez, CA, USA, MW cutoff = 1 kDa, 3.5 kDa, 12-14 kDa for HCC-PEG, HCC-4arm PEG and HCC-8arm PEG, respectively). The dialysis was performed for 48 h using the same Milli-Q water/DMSO mixture as releasing medium and for 4 h using only Milli-Q water. Finally, the solutions were freeze-dried and the HCC-conjugated polymers were obtained as yellow solids (HCC-PEG yield: 0.82 g, 75%; HCC-4arm PEG yield: 1.05 g, 91%; HCC-8arm PEG yield: 0.99 g, 93%).

Chemical characterization of HCC-PEG conjugates

The HCC-PEG conjugates underwent UV-Vis spectroscopic characterization. HCC-PEG, HCC-4arm PEG and HCC-8arm PEG were dissolved in PBS, pH 7.4 at a concentration of 10 mg/mL and diluted to 0.1 mg/mL using the same buffer. The UV-Vis absorption spectra were recorded using an Evolution 201 UV-Vis spectrophotometer (Thermo Fisher Scientific, Waltham, MA, USA) in the wavelength range of 250-450 nm.

For ¹H NMR spectroscopic characterization, ¹H NMR spectra of HCC-PEG, HCC-4arm PEG and HCC-8arm PEG were recorded in deuterated chloroform using an AVANCE III 400 Ultrashield spectrometer (Bruker, Billerica, MA, USA). NMR data were processed with MestreNova 6.2.0 Software (Mestrelab Research SL, Santiago de Compostela, Spain). The chemical identity of HCC-conjugated polymers was assessed by identifying the characteristic signals of PEG and HCC, as follows:

- HCC-PEG. ¹H NMR (CDCl₃, 400 MHz), δ (ppm): 3.38 (s, 3H, CH₃O-PEG), 3.64 (bs, ~180H, -CH₂CH₂O- of PEG chain), 6.88-6.90 (m, 2H, Ar-H of HCC), 7.51 (d, 1H, =CH of HCC), 8.79 (s, 1H, =CH of HCC), 9.03 (bs, 1H, -CONH-PEG).
- HCC-4arm PEG. ¹H NMR (CDCl₃, 400 MHz), δ (ppm): 3.64 (bs, ~225H, -CH₂CH₂O- of PEG chain), 6.88-6.90 (m, 2H, Ar-H of HCC), 7.51 (d, 1H, Ar-H of HCC), 8.79 (s, 1H, =CH of HCC), 9.03 (bs, 1H, -CONH-PEG).
- HCC-8arm PEG. ¹H NMR (CDCl₃, 400 MHz), δ (ppm): 3.64 (bs, ~225H, -CH₂CH₂O- of PEG chain), 6.88-6.90 (m, 2H, Ar-H of HCC), 7.51 (d, 1H, Ar-H of HCC), 8.79 (s, 1H, Ar-H of HCC), 9.03 (bs, 1H, -CONH-PEG).

FT-IR analysis was performed. HCC-PEG, HCC-4arm PEG and HCC-8arm PEG samples were thoroughly ground with KBr, pellets were prepared by compression and analyzed by FT-IR

spectroscopy using a SPECTRUM BXII FTIR (Perkin Elmer, Waltham, MA, USA) with a resolution of 4 cm⁻¹. mPEG-NH₂ was used as control.

- mPEG-NH₂ FT-IR: ν 3413, 2887, 1467, 1360, 1343, 1280, 1242, 1149, 1113, 1060, 963, 947, 842, 529 cm⁻¹.
- HCC-PEG FT-IR: ν 3367, 2887, 1718, 1546, 1466, 1360, 1343, 1280, 1242, 1149, 1113, 1060, 963, 842, 528 cm⁻¹.
- HCC-4arm PEG FT-IR: ν 3448, 2885, 1707, 1541, 1466, 1360, 1344, 1281, 1242, 1147, 1113, 1061, 963, 842, 520 cm⁻¹.
- HCC-8arm PEG FT-IR: ν 3455, 2885, 1708, 1542, 1466, 1360, 1344, 1281, 1242, 1147, 1113, 963, 842, 519 cm⁻¹.

Assessment of conjugation yield of HCC-PEG, HCC-4arm PEG and HCC-8arm PEG samples was performed by spectrophotometric analysis. Samples were dissolved in Milli-Q water and diluted in 0.1 M borate buffer, pH 8.3. HCC was quantified by spectrophotometric analysis at 410 nm, referring to a calibration curve obtained with standard solutions of HCCA-NHS. PEG in solution was quantified by iodine assay⁶¹. Briefly, Milli-Q HCC-PEG, HCC-4arm PEG and HCC-8arm PEG samples were diluted to 0.01 mg/mL with Milli-Q water and 1 mL of diluted samples were added of 250 μ L barium chloride (5% w/v in 1 M HCl) and 250 μ L iodine solution (1.27 g of I₂ in a 2% KI solution in Milli-Q water). After 15 min, absorbance was measured at 535 nm and referred to a calibration curve of mPEG-NH₂ obtained with the same procedure. The conjugation yield (reported as %) of HCC-PEG, HCC-4arm PEG and HCC-8arm PEG was calculated by the [HCCA]/[PEG] molar ratio compared to the maximum theoretical molar ratio ([HCCA]/[PEG] of 1:1 for HCC-PEG, [HCCA]/[PEG] of 4:1 for HCC-4arm PEG and [HCCA]/[PEG] of 8:1 for HCC-8arm PEG). The conjugation yield was estimated to be 92% for HCC-PEG, 95% for HCC-4arm PEG, 90% for HCC-8arm PEG.

The absence of free unconjugated HCCA in the samples was tested by reversed phase high-performance liquid chromatography (RP-HPLC). The analysis was performed using a Jupiter analytic column (C18, 5 μ , 300 Å , 250 x 4.6 mm, Phenomenex, Torrance, CA, USA) eluted with a linear gradient of water/acetonitrile containing 0.1 % (v/v) trifluoroacetic acid from 95% to 5% water/acetonitrile over 40 min. The flow rate was set at 1.0 mL/min and the UV-Vis detector at 360 nm.

Synthesis of HCC-Gelatin (HCC-Gel) conjugate

HCCA (100 mg, 0.49 mmol) was dissolved in anhydrous DMSO (2 mL), then NHS (112 mg, 0.97 mmol) and DCC (200 mg, 0.97 mmol) were added to the solution. The reaction mixture was stirred overnight in the dark and filtered to remove the insoluble dicyclohexylurea. The 7-hydroxycoumarin-3-carboxylic acid N-succinimidyl ester (HCCA-NHS) was isolated by precipitation in diethyl ether (45 mL). The precipitate was rinsed with diethyl ether (30 mL \times 3) and finally desiccated under vacuum.

Gelatin (1.00 g, 0.01 mmol) was dissolved in anhydrous DMSO (30 mL) at 50 °C, then triethylamine (22.30 μ L, 0.16 mmol) and HCCA-NHS (49 mg, 0.16 mmol) were added to the solution. After 12 h stirring at 50 °C in the dark, the reaction mixture was diluted with 50 mM phosphate, pH 7.4 (120 mL) and dialysed with a Spectra/Por dialysis membrane (SpectrumLabs, Rancho Dominguez, CA, USA, MW cutoff = 12-14 kDa). The dialysis was performed for 36 h using a 9:1 (v/v) 50 mM phosphate/DMSO mixture as releasing medium and for 4 h using only

Milli-Q water. Finally, the solution was freeze-dried and the HCC-Gel conjugate was obtained as yellow solid (yield: 0.99 g, 96%).

Chemical characterization of HCC-Gel conjugate

5 The HCC-Gel conjugate underwent size exclusion chromatography (SEC). HCC-Gel was dissolved in PBS, pH 7.4 at 0.4 mg/mL. HCCA, used as reference, was dissolved in DMSO at 5.0 mg/mL and diluted to 5 μ g/mL in PBS, pH 7.4. The analysis was performed using an AS-1555 HPLC system (Jasco, Tokyo, Japan) equipped with a PU-2089 Plus pump, a UV-2077 Plus detector and a Zorbax GF-250 column (4 μ m, 4.6 x 250 mm, Agilent Technologies, Santa Clara, CA, USA) eluted with 63 mM phosphate, 150 mM NaCl, pH 7.4. The flow rate was set at 0.3 mL/min and the UV-Vis detector at 400 nm for coumarin detection.

10 The amount of HCC in HCC-Gel sample was quantified by spectrophotometric analysis. The sample was dissolved in 0.1 M borate buffer, pH 8.3 and analyzed at 410 nm, referring to a calibration curve of HCCA-NHS. Gelatin quantification in the conjugate was performed by BCA protein assay (Sigma-Aldrich). The absorbance was measured at 562 nm and referred to a calibration curve of Gelatin obtained with the same procedure.

15 The conjugation yield (reported as %) of HCC-Gel was calculated by the [HCCA]/[gelatin] molar ratio compared to the maximum theoretical molar ratio ([HCCA]/[Gel] of 26:1). The gelatin conjugation yield was estimated to be 20% (5.2:1 [HCCA]/[Gel] molar ratio).

20 The maximum theoretical [HCCA]/[Gel] molar ratio was calculated on the basis of the content of primary amino groups of gelatin, which was assessed by TNBS assay⁶². Briefly, 160 μ L of a 15.74 μ M Gel solution in 0.1 M borate buffer, pH 9.3 were added to 810 μ L of the same buffer followed by 30 μ L of TNBS (5% w/v in mMilli-Q water). After 30 min, the absorbance was measured at 420 nm. The amount of free amino groups was assessed using a calibration curve obtained with Gly-Gly, using the same procedure.

Synthesis of CMMC-4arm PEG and CMMC-Gelatin (CMMC-Gel) conjugate

30 CMMC (100 mg, 0.43 mmol) was dissolved in anhydrous DMSO (2 mL), then NHS (98 mg, 0.85 mmol) and DCC (176 mg, 0.85 mmol) were added. The reaction mixture was stirred overnight in the dark and filtered to remove the insoluble dicyclohexylurea. The 7-(carboxymethoxy)-4-methylcoumarin N-succinimidyl ester (CMMC-NHS) was isolated by precipitation in diethyl ether (45 mL). The precipitate was rinsed with diethyl ether (30 mL \times 3) and finally desiccated under vacuum.

35 For PEG conjugation, 10 kDa 4-arm PEG amine pentaerythritol core (4arm-PEG-NH₂, 1.0 g, 0.10 mmol) was dissolved in anhydrous DMSO (10 mL), then the reaction mixture was added of triethylamine (55.75 μ L, 0.40 mmol) and CMMC-NHS (0.27 g, 0.80 mmol). After 12 h stirring at room temperature in the dark, the reaction mixtures were added dropwise to diethyl ether (300 mL). The precipitates were recovered by centrifugation at 4000 rpm and dried under vacuum. The crude products were dissolved in a 9:1 (v/v) water/DMSO mixture and dialysed using Spectra/Por dialysis membranes (MW cutoff = 3.5 kDa, 12-14 kDa for CMMC-4arm PEG and CMMC-8arm PEG respectively). The dialysis was performed for 48 h using the same water/DMSO mixture as releasing medium and for 4 h using only water. Finally, the solutions were freeze-dried, and the CMMC-conjugated polymers were obtained as solids (CMMC-4arm PEG yield: 1.02 g, 94%).

45 For gelatin conjugation, gelatin (1.00 g, 0.01 mmol) was dissolved in anhydrous DMSO (30 mL) at 50 $^{\circ}$ C, then triethylamine (22.30 μ L, 0.16 mmol) and CMMC-NHS (53 mg, 0.16 mmol) were added to the solution. After 12 h stirring at 50 $^{\circ}$ C in the dark, the reaction mixture was diluted with

50 mM phosphate, pH 7.4 (120 mL) and dialysed with a Spectra/Por dialysis membrane (SpectrumLabs, Rancho Dominguez, CA, USA, MW cutoff = 12-14 kDa). The dialysis was performed for 36 h using a 9:1 (v/v) 50 mM phosphate/DMSO mixture as releasing medium and for 4 h using only Milli-Q water. Finally, the solution was freeze-dried and the CMMC-Gel conjugate was obtained as white solid (yield: 0.95 g, 92%).

Chemical characterization of CMMC-4arm PEG conjugate

The CMMC- 4 arm PEG conjugates underwent UV-Vis spectroscopic characterization. CMMC-4arm PEG was dissolved at 10 mg/ml in phosphate buffer (PBS), pH 7.4 and diluted 1:100 in the same buffer. The absorption spectra were recorded on an Evolution 201 UV-Vis spectrophotometer (Thermo Fisher Scientific, Waltham, MA, USA) in the wavelength range of 250-450 nm.

For ¹H NMR spectroscopic characterization, ¹H NMR spectra of CMMC-4arm PEG was recorded in deuterated chloroform using an AVANCE III 400 Ultrashield spectrometer (Bruker, Billerica, MA, USA). NMR data were processed with MestreNova 6.2.0 Software (Mestrelab Research SL, Santiago de Compostela, Spain). The composition of CMMC-conjugated polymers was assessed by identifying the characteristic peaks of PEG and CMMC units, as follows:

- CMMC-4arm PEG. ¹H NMR (CDCl₃, 400 MHz), δ (ppm): 2.41 (d, 3H, ArCH₃ of coumarin), 3.64 (bs, ~900H, -CH₂CH₂-O- of PEG chain), 4.56 (s, 2H, -NHCO-CH₂-O- of coumarin), 6.17 (s, 1H, ArH of coumarin), 6.85 (d, 1H, ArH of coumarin), 6.91 (dd, 1H, ArH of coumarin), 7.05 (bs, 1H, -CONH-PEG), 7.55 (d, 1H, ArH of coumarin).

Quantification of conjugation degree of CMMC-4arm PEG was assessed by using a spectrophotometric assay by absorbance at 320 nm in 0.1 M phosphate buffer, pH 7.4 and referring to a calibration curve obtained with standard solutions of CMMC. For PEG quantification, iodine assay was used. Briefly, each conjugate was dissolved in milli-Q water and diluted to 0.01 µg/mL. Barium chloride (5% w/v in 1 M HCl) and iodine solution (1.27 g of I₂ in a 2% KI solution in Milli-Q water) were added 1:4 to CMMC-4arm PEG. After 15 min, absorbance was measured at 535 nm and referred to a calibration curve of mPEG-NH₂ obtained with the same procedure.

The absence of free unconjugated CMMC in the samples was tested by reversed phase high-performance liquid chromatographic (RP-HPLC). The analysis was performed on a Jupiter analytic column (C18, 5 µ, 300 Å, 250 x 4.6 mm, Phenomenex, Torrance, CA, USA) eluted with a linear gradient of water/acetonitrile containing 0.1 % (v/v) trifluoroacetic acid over 40 min. The flow rate was set at 1.0 mL/min and the UV-Vis detector at 320 nm. The conjugation yield (reported as %) of CMMC-4arm PEG was calculated by the [CMMC]/[PEG] molar ratio compared to the maximum theoretical molar ratio ([CMMC]/[PEG]) of 4:1 for CMMC-4arm PEG. The conjugation yield was estimated to be 94% for CMMC-4arm PEG.

Chemical characterization of CMMC-Gel conjugate

CMMC-Gel conjugate underwent size exclusion chromatography (SEC). CMMC-Gel was dissolved in PBS, pH 7.4 at 0.4 mg/mL. CMMC, used as reference, was dissolved in DMSO at 5.0 mg/mL and diluted to 5 µg/mL in PBS, pH 7.4. The analysis was performed using an AS-1555 HPLC system (Jasco, Tokyo, Japan) equipped with a PU-2089 Plus pump, a UV-2077 Plus detector and a Zorbax GF-250 column (4 µm, 4.6 x 250 mm, Agilent Technologies, Santa Clara, CA, USA) eluted with 63 mM phosphate, 150 mM NaCl, pH 7.4. The flow rate was set at 0.3 mL/min and the UV-Vis detector at 320 nm for coumarin detection.

The amount of CMMC in CMMC-Gel sample was quantified by spectrophotometric analysis. Samples dissolved in 0.1 M phosphate buffer pH 7.8 were analyzed at 320 nm, referring to a calibration curve of CMMC. Gelatin quantification in the conjugate was performed by BCA protein assay (Sigma-Aldrich). The absorbance was measured at 562 nm and referred to a calibration curve of Gelatin obtained with the same procedure.

The conjugation yield (reported as %) of CMMC-Gel was calculated by the [CMMC]/[gelatin] molar ratio compared to the maximum theoretical molar ratio ([CMMC]/[Gel] of 26:1). The gelatin conjugation yield was estimated to be 18% (4.7:1 [HCCA]/[Gel] molar ratio).

The quantification of the maximum theoretical molar ratio was derived as reported above.

Characterization of HCCA [2+2] cycloaddition reaction by ¹H NMR spectroscopy and electrospray ionization time-of-flight mass spectrometry (ESI-TOF MS)

HCCA in solution was used to confirm the [2+2] cycloaddition reaction of HCCA-conjugated polymers.

A 60 mg/mL solution of HCCA in deuterated DMSO (80 μL) was irradiated with a 365 nm lamp (BlueWave 50 UV light lamp). The solution was irradiated at 1 cm distance for 1 h and analyzed before and after irradiation by ¹H NMR spectroscopy with a Bruker DMX 600 spectrometer (Billerica, MA, USA) and by ESI-TOF-MS with an Applied Biosystems Mariner ESI-TOF spectrometer (Monza, MI, Italy). HCCA monomers and dimers were identified by the characteristic signals in the ¹H NMR spectra, as follows:

- HCCA solution before irradiation. ¹H NMR (DMSO-d₆, 600 MHz), δ (ppm): 6.73 (d, 1H, Ar-H of HCCA monomer), 6.84 (dd, 1H, Ar-H of HCCA monomer), 7.74 (d, 1H, Ar-H of HCCA monomer), 8.68 (s, 1H, =CH of HCCA monomer), 11.07 (bs, 1H, OH of HCCA monomer), 12.86 (bs, 1H, COOH of HCCA monomer).
- HCCA solution after UV irradiation. ¹H NMR (DMSO-d₆, 600 MHz), δ (ppm): 4.63 (s, 1H, cyclobutyl-CH of HCCA dimer), 6.38 (d, 1H, Ar-H of HCCA dimer), 6.62 (dd, 1H, Ar-H of HCCA dimer), 6.73 (d, 1H, Ar-H of HCCA monomer), 6.84 (dd, 1H, Ar-H of HCCA monomer), 7.03 (d, 1H, Ar-H of HCCA dimer), 7.74 (d, 1H, Ar-H of HCCA monomer), 8.68 (s, 1H, =CH of HCCA monomer), 11.07 (s, 1H, OH of HCCA monomer), 12.86 (bs, 1H, COOH of HCCA monomer).

Before and after irradiation, the HCCA solution in DMSO underwent ESI-TOF analysis.

- HCCA solution before irradiation. ESI-TOF: m/z [M - H]⁻ calcd for HCCA monomer 205.02; found 205.02.
- HCCA solution after UV irradiation. ESI-TOF: m/z [M - H]⁻ calcd for HCCA monomer 205.02; found 205.02. m/z [M - H]⁻ calcd for HCCA dimer 411.30; found 409.02, consistent with the formation of HCCA dimer undergoing a keto-enol tautomerism induced by the gas-phase ionization.

Transmission electron microscopy (TEM) analysis of HCC-PEG self-assembled nanostructures

A 20 mg/mL HCC-PEG solution in Milli-Q water was diluted to 0.5 mg/mL with Milli-Q water and placed on a carbon coated copper grid. After the removal of the volume excess with a filter paper, the samples were negatively stained with uranyl acetate (2% in distilled water) for 5 min at room temperature and analyzed using a Tecnai G2 transmission electron microscope (FEI, Oregon, USA). A solution of mPEG-NH₂ was used as negative control and treated with the same procedure.

Analysis of HCC-PEG after single-photon or two-photon (2P) irradiation.

For single photon excitation, HCC-PEG was dissolved in PBS, pH 7.4 at 20 mg/mL. The solution (20 μ L) was irradiated with a BlueWave 50 UV light lamp (Dymax Corporation, Torrington, CT, USA) at 365 nm for 1, 2, 3, 4, 5, 6, 7, 8, 9, 10, 20 and 30 min. The dimerization degree was calculated, given the absorbance of the samples at 403 nm, before and after irradiation, by using the following equation:

$$\text{Dimerization (\%)} = \left(1 - \frac{A_t}{A_0}\right) \times 100$$

where A_0 is the absorbance of the sample before irradiation, while A_t is the absorbance of the samples after irradiation, both measured at 403 nm, i.e. the wavelength of the maximum absorption peak.

To test that PEG doesn't interfere with the absorbance of coumarin moiety, a solution of mPEG-NH₂ was prepared in PBS, pH 7.4 at 20 mg/mL and treated with the same procedure. No absorbance was measured at 403 nm before and after irradiation.

For 2P irradiation, HCC-PEG was patterned onto HCCA-functionalised glass coverslips following the highly spatially localized 2P excitation given by a multi-photon laser-scanning microscope. HCCA-functionalization on coverslip was achieved as follows. Coverslip was cleaned and extensively rinsed with deionized water and finally oxidized by the PDC-002-CE Plasma Cleaner (Harrick Plasma, Ithaca, NY, USA) for 30 s. The glass slide was incubated in a 2% (v/v) APTES solution in absolute ethanol (300 μ L) under gently stirring. After 6 min, the substrate was washed 3 times with ethanol to remove unbound APTES and finally dried at 110° C for 2 h. The glass slide was treated with 300 μ L of a 5 mg/mL solution of HCCA-NHS in anhydrous DMSO added of a catalytic amount of TEA. The reaction mixture was maintained under stirring overnight at room temperature in the dark. Finally, coverslip was washed 3 times with DMSO, Milli-Q water, absolute ethanol and dried under a nitrogen stream. To assess each functionalization step, the glass slide was characterized by static contact angle analysis using a DSA 30 Drop Shape Analysis System (KRUSS GmbH, Hamburg, Germany). For 2P irradiation, HCC-PEG solution (1 mg/mL in PBS) was drop-cast onto the coverslip previously functionalised with HCCA. 2P microscopy was used to irradiate surfaces in contact with HCC-PEG solution and produce 2P crosslinked area of 850x850 μ m², 425x425 μ m² and 280x280 μ m² (laser wavelength of 800 nm; laser power 0.7 mW measured before objective back aperture; writing time of 1.14 ms/line and rate of 1.72 frame/s; 4 frame per plane). After photo-exposition, samples were washed with PBS, fixed in 4% (w/v) paraformaldehyde (PFA, Sigma-Aldrich) in PBS for 7 min at room temperature and maintained at 4 °C in PBS, then processed for immunofluorescence analysis (see Section 14) and confocal imaging acquisition.

HCC-4arm PEG, HCC-8arm PEG and HCC-Gel 2P hydrogel crosslinking.

With the aim to provide glass surface HCCA-groups for covalent bonding HCC-branched polymers solutions were drop-cast onto glass coverslip previously functionalized with HCCA—as described in Section 10. HCC-4arm PEG and HCC-8arm PEG were dissolved in PBS (300 mg/mL) at room temperature under agitation. HCC-Gel was dissolved in PBS (100 mg/mL) under agitation at 60 °C for 10 min. When coverslips were used, a second coverslip was placed on top of the drop of HCC-polymeric solutions to limit water evaporation during the irradiation process. For crosslinking reaction analysis, HCC-Gel solution was prepared at the following concentrations, 100 mg/mL, 120 mg/mL, 140 mg/mL, 160 mg/mL, 180 mg/mL and 200 mg/mL. HCC-Gel or

HCC-Gel were also mixed in a 50/50 ratio with Matrigel or loaded into pre-gelified Matrigel, as specified above. 2P hydrogel crosslinking was achieved by using Scientifica 2-Photon microscope. Specific working conditions are reported in **Suppl. Table S3-S6**. Laser power is measured before objective back aperture, corresponding to about 1% of the power on the sample plane. In a typical working condition, standard line scan velocity was 0.8 mm/ms, pixel dwell time 2 μ s and z spacing 1 μ m. The time required to polymerize a volume of 1 mm³ is about 30 min.

CMMC-4arm PEG and CMMC-Gel UV-mediated hydrogel crosslinking.

For crosslinking reaction analysis, 5 μ L CMMC-4 arm PEG (300 mg/mL) or CMMC-Gel (100 mg/mL) solution was located in a humid chamber at 3 cm from a 365nm UV LED Gen 2 Emitter LZ4-04UV00 (Led Engin) and irradiated for different minutes as reported. When CMMC-Gel solution was analyzed at different concentrations (100 mg/mL, 120 mg/mL, 140 mg/mL, 160 mg/mL, 180 mg/mL and 200 mg/mL), 5 μ L of solution was located in a humid chamber at 3 cm from a 365nm UV LED Gen 2 Emitter LZ4-04UV00 (Led Engin) and irradiated for 3 minutes.

Atomic Force Measurement (AFM)

After development in PBS, HCC-4arm PEG and HCC-Gel hydrogels (212 μ m x 212 μ m x 150 μ m) or were maintained in PBS. For HCC-Gel/Matrigel 3D structure measurements, Matrigel was dissociated with cold PBS-EDTA solution (0.5mM EDTA, Invitrogen #AM9260G) under gentle agitation overnight at 4°C. For cell-laden HCC-Gel constructs, samples were prepared as reported above and maintained into PBS for further analysis. All the samples were analyzed by using an Atomic Force Microscope, mounted on an Inverted Optical Microscope (XEBio, Park Systems, Korea). This combination enabled positioning of the AFM tip on the area of interest of the samples. All force-displacement curves were collected using PPP-CONTSCR-10 pyramidal tips mounted on Si₃N₄ cantilevers with a nominal spring constant of 0.2 N/m (NanoSensors, Neuchatel, Switzerland). Cantilever spring constants were calibrated by the manufacturer prior to use. Indentations were performed at a rate of 0.2 μ m/s. All AFM measurements were done in a fluid environment (PBS) at room temperature.

The Young's modulus was calculated applying a fit of the Hertz model to the force curve, assuming a Poisson ratio of 0.5. The moduli of at least 3 samples of each lot were calculated as an average over 3-5 sites per sample.

Cell cultures

HUVECs were transduced with a lentiviral vector encoding for eGFP⁶³ and cultured in Endothelial Growth Media (EGM, Lonza). For 2D culture on hydrogel, 20 x 10⁴ cells were seeded onto HCC-Gel structures (fabrication details reported in **Suppl. Table S4**), located in a 12 multiwell culture dish and cultured for 24 h at 37 °C and 5% CO₂ in cell incubator.

Neural stem cell (NSC)/neural progenitor cell (NPC) culture were derived from human embryonic stem cells (hESCs). Briefly, hESCs were detached using Dispase and plated in low-adhesion dishes to generate embryoid bodies (EB) in the presence of two small molecules, SB-431542 (10 μ M) and Dorsomorphin (DSO, 3 μ M), which inhibit TGF β and BMP respectively, and Rock-inhibitor (10 μ M, Miltenyi Biotec). After 5 days in culture, EBs were collected and plated on Matrigel coated dishes in EB medium supplemented with DSO (1 μ M) and Fgf-2 (10 ng/ml) to obtain neural rosette. On day 6 EB medium was changed to N2 medium with DSO and Fgf-2 and changed daily until neural rosettes were formed. On day 12 after seeding, neural rosettes were picked and grown in suspension for 2 days in N2 medium with Fgf-2 (20 ng/ml). Finally, on day 14, floating rosettes

were collected, digested with 0,025% Trypsin-EDTA and plated on tissue culture petri dish coated with poly-ornithine/laminin in N2 medium with Fgf-2 (10 ng/ml), Egf (10 ng/ml) and B27 supplement (1:1000) to obtain a NSC/NPC line. NSCs/NPCs were split with 0,025% Trypsin-EDTA every 3 days at 1:2/1:3 ratio. EB medium: DMEM/F-12 (Dulbecco's Modified Eagle Medium/Nutrient Mixture F-12, Thermofisher #11320-033), KSR 20% (Thermofisher), b-Mercaptoethanol 1:1000 (Gibco), Non-Essential Amino Acids (NEAA) 1:100 (Gibco), L-Glutamine 1:100 (Thermofisher Scientific, #25030024). N2 medium: DMEM/F-12 (Dulbecco's Modified Eagle Medium/Nutrient Mixture F-12, Thermofisher #11320-033), N-2 supplement 1% (Thermofisher) and D-glucose (Thermofisher, 350µl/100 ml). For 2D culture on hydrogel, 3.2×10^5 cells were seeded onto HCC-Gel structures (fabrication details reported in **Suppl. Table S4**), located in a 12 multiwell culture dish and cultured for 3 days at 37 °C and 5% CO₂ in cell incubator. After culture, cells were fixed in 4% (w/v) paraformaldehyde (PFA, Sigma-Aldrich) in PBS for 7 min at room temperature and maintained at 4 °C in PBS until use.

Primary muscular fibroblasts (FBs) were isolated from wild-type or transgenic C57BL/6-(ACTB-EGFP)/J mice as previously described⁶⁴. Upon 3 passages of expansion, cells were transduced with a lentiviral vector encoding for mCherry⁶³. After 2 passages, mCherry⁺FBs were purified through Fluorescence Assisted Cell Sorting (FACS) at the Flow Cytometry BD FACS Aria IIIu, based on the epifluorescence signal. Only mCherry⁺FBs were collected and further expanded. For 3D cell laden culture, 10^4 cells were seeded into Matrigel, or Matrigel or CMMC-Gel exposed to UV light for 3 minutes at an irradiation distance of 3 millimeters, located in a 24 multiwell culture dish, cultured for 2 days at 37 °C and 5% CO₂ in cell incubator before performing cell viability assay as described above. For 2P cell-laden HCC-Gel 3D bioprinting, 4×10^4 mCherry⁺FBs or wild-type FBs were resuspended in 10 µL of HCC-Gel solution, drop cast on glass coverslip and processed as described in **Suppl. Table S4**. 2P-cell laden constructs were analyzed by imaging or AFM as described above.

Muscle stem cell-derived cells (MuSCs) were isolated from wild-type or transgenic C57BL/6-(ACTB-EGFP)/J mice as previously described⁶⁴. Cells were expanded for 1 passage at 37 °C in cell incubator, using proliferating medium composed by DMEM supplemented with 20% horse serum, 10% fetal bovine serum (Gibco), 1% chicken embryo extract (Sera Laboratories International), bFGF (25ng/µl, Invitrogen #PHG0264) and 1% Pen/Strep (Thermofisher). For 2P cell-laden 3D bioprinting, 2×10^4 MuSCs were resuspended in 5 µL of HCC-Gel solution, drop cast on glass coverslip and processed as described in **Suppl. Table S4**. For 3D cell-laden culture, 1×10^4 cells were seeded into Matrigel, or CMMC-Gel exposed to UV light for 3 minutes at an irradiation distance of 3 millimeters. Samples were located in a 24 multiwell culture dish, cultured for 2 days at 37 °C and 5% CO₂ in cell incubator before performing cell viability assay as described above. For 2P cell-laden HCC-Gel 3D bioprinting, 2×10^4 MuSCs were resuspended in 10 µL of HCC-Gel solution, drop cast on glass coverslip and processed as described in **Suppl. Table S4**. Samples were cultured in proliferating media and analyzed 2 days after 3D bioprinting (cell directionality was quantified as reported above). For long term 3D culture, 2×10^4 cells were seeded onto 3D elongated-shaped HCC-Gel 2P crosslinked hydrogels (as described in **Suppl. Table S4**). After 5 days of culture in proliferating medium, differentiation medium (DMEM supplemented with 2% horse serum and 1% Pen/Strep) was used for the following 5 days of cell culture. After 10 days, samples were fixed in 4% (w/v) paraformaldehyde (PFA, Sigma-Aldrich) in PBS for 7 min at room temperature and maintained at 4 °C in PBS until use.

Human small intestinal crypt stem cells were isolated from a small intestine pediatric biopsy following a well-established dissociation protocol^{65,66}. Isolated crypts were cultured in pure Matrigel growth factor reduced (BD 354230) droplets and expanded in WENR media of a base AddMEM+++ : Advanced DMEM F-12 (Thermo 12634), 10mM HEPES (Thermo 15630080), 2mM Glutamax (Thermo 35050061), 1% Pen/Strep (Thermo 15140122) supplemented with B-27 supplement minus vitamin A (Thermo 12587010), 1.25mM n-acetylcysteine (Sigma A9165), Pen/Strep (Thermo 15140122), 100 ng/mL Wnt-3A (Peprotech 315-20), 500 ng/mL R-spondin 1 (Peprotech 120-38), 100 ng/mL Noggin (R&D 6057-NG), 50 ng/mL EGF (Thermo PMG8043), 10 nM Gastrin (Sigma G9020), 3 μ M GSK-3 inhibitor (CHIR 99021) (Tocris 4423), 500 nM TGF β inhibitor (A83-01) (Sigma SML0788), 10 μ M P38 inhibitor (SB202190) (Sigma S7067), 10 nM Prostaglandin E2 (Cambridge cay14010). When indicated, small intestinal enteroids were transfected with lentiviral vector for Green Fluorescent Protein (GFP^{*}). Enteroids were passaged every 6-8 days by 5 min TrypLE (Thermo 12605010) dissociation and seeded in new Matrigel droplets. For the multi-photon experiments, hSIOs that were recently passaged (1-2 days) were washed thoroughly from the old Matrigel with cold AddMEM+++. Cells were pelleted at 400 g and supernatant discarded. For HCC-Gel/Matrigel 50/50 experiments, HCC-Gel 10% solution was liquefied at 60 °C for 5 min and quickly mixed 1:1 to liquid matrigel at 4 °C to form a pre-gel with final concentration of 5% HCC-Gel and 50% Matrigel. Cell pellet was quickly resuspended in the pre-gel mixture and the droplets were allowed to solidify for 15 min at 37 °C, before proceeding to 2P crosslinking (as described in **Suppl. Table S5**). Alternatively, for experiments in which HCC-Gel or HCC-PEG was loaded into gelified Matrigel, cells were pelleted at 400 g, replated in 5 μ l drops in the well-plate and let the Matrigel polymerize at 37°C for 5 minutes, then 5 μ l of HCC-solution was added onto the gelified Matrigel and incubated at 37°C for 10 minutes, before proceeding to 2P crosslinking (as described in **Suppl. Table S5**). After 2P printing, samples were cultured for 2, 3, 6 or 8 days in the above WENR media before being use for analysis. For basal/apical ratio⁶⁷ and basal/apical major axis⁶⁶, measurements were performed on confocal fluorescence images stained for nuclei and actin by using ImageJ software (Feret's angle was quantified as reported above).

Cell viability assay

For cell viability assay on organoids, cells were passaged to solution and seeded in quadruplicates. Enteroids were expanded for 2 days in HCC-Gel/Matrigel 50:50 solution, or for 2 or 8 days after HCC-Gel or for 2 days after HCC-PEG 2P-crosslinking. For cell viability assay on FBs or MuSCs, 2P cell-laden bioprinted constructs and 3D cultures were maintained for 2 days in culture. Viability assay was performed using LIVE/DEADTM Viability/Cytotoxicity Kit, for mammalian cells (Thermo L3224), following supplier instructions. Briefly, organoids were washed with basal DMEM F-12 and incubated in basal medium with Hoechst (Thermo H139910 μ g/mL), calcein-AM (3 μ M) and ethidium homodimer-1 (3 μ M). Cells in Matrigel droplets were washed twice and analyzed by fluorescence imaging.

Tissue preparation and histological analysis staining.

The tissue samples were embedded in O.C.T. cryomold (VWR Q-Path Chemicals, VWRQ00411243) and placed in cryostat (Leica 1860 cryostat) at -24°C. Cross or longitudinal cryo-sections (10 μ m thick) were first air-dried, then processed for staining. Hematoxylin & eosin (Bio-Optica, Bio-Optica Milano Spa, 04-061010) or Masson's Trichrome Stain (Bio-Optica, Bio-

Optica Milano Spa, 04-010802) were performed following manufacturing instructions. Samples were examined under a light microscope (Olympus BX60 microscope).

Investigation of apoptosis.

In vitro cultures and tissues cryo-sections were fixed with 4% paraformaldehyde (PFA, Sigma, P6148) and Terminal deoxynucleotidyl transferase (TdT) dUTP Nick-End Labeling (TUNEL) assay was performed using the Click-iT Tunel Alexa Fluor 594 Imaging Assay (Invitrogen, C10246). Randomly chosen visual fields were observed under a 20x objective by epifluorescence or confocal imaging.

Immunofluorescence analysis.

For *in vitro* cultures and tissues cryo-sections, samples were fixed in 4% PFA and blocked using PBS-Triton 0.5% with bovine serum albumin 1% (BSA, Gibco). For Matrigel droplets with embedded enteroids and 2P printed geometries, samples were fixed in 2% glutaraldehyde dissolved in PBS with Ca²⁺/Mg²⁺ for 1 h at room temperature, and then washed. When required, samples were incubated 1 hour at room temperature in NH₄Cl 0.1M in PBS to reduce hydrogel autofluorescence. Samples were incubated in blocking solution 1 h at 37 °C or overnight at +4 °C with the primary antibody. Secondary antibody and eventually phalloidin-647 (ThermoFisher, A22287) were incubated in blocking buffer for 1 h at room temperature (2 h at 37 °C for cultured organoids). Samples were analyzed by confocal imaging (Leica TCS SP5 microscope). The following primary antibodies were used: 1:100 Rat anti- α -Laminin (Sigma, L0663), 1:50 Rabbit anti-GFP (Invitrogen, A11122), 1:25 Mouse anti-eMyHC (DSHB, F1.652-s), 1:100 Rabbit anti-F4/80 (Santa Cruz Biotechnology, sc-25830), 1:25 Rabbit anti-MyoG (Santa Cruz Biotechnology, sc-576), 1:100 Rabbit anti-Human Ezrin (Thermo, PA5-29358); 1:100 Rat anti-integrin beta-4 (Abcam, ab110167); 1:50 Mouse anti-PEG (GenScript, 5E10E9); 1:500 Mouse anti-hNestin (Millipore, MAB 5326); 1:5000 Mouse anti-BIII-Tubulin (Tuj1 – Biolegend, 801202); 1:50 Goat anti-Sox1 (R&D, AF3369); 1:200 Rabbit anti-Pax6 (Biolegend, 901301); 1:2000 Rabbit anti-p75 (Promega, G323A); 1:1000 Goat anti-GFAP (Abcam, ab53554); 1:10 Goat anti-collagen I (SouthernBiotech, 1310-01); 1:50 Rabbit anti-caspase-8 p18 (H-134; Sigma, sc-7890). The following secondary antibodies were used: 1:200 Donkey anti-mouse 488 (ThermoFisher, A21202); 1:200 Donkey anti-rabbit 488 (ThermoFisher, A21206); 1:200 Donkey anti-mouse 594 (ThermoFisher, A21203); 1:200 Donkey anti-rabbit 594 (ThermoFisher, A31573); 1:500 Goat anti-mouse 594 (ThermoFisher R37121); 1:500 Goat anti-Rabbit 568 (ThermoFisher, A-11011); 10 μ g/mL Hoechst 33342 (ThermoFisher, H1399); 1:100 Goat anti-Rat Cy2 (Jackson, 112-225-167).

Intravital HCC-4arm PEG, HCC-8arm PEG, HCC-Gel 3D printing and intravital HCC-Gel bioprinting.

Mice were anaesthetized using *i.p.* injection of Zoletil® 50/50 (40 mg/kg) and Rompun® 2% Xilazina (5 mg/kg) in physiologic solution. Induction of deep surgical anaesthesia was confirmed by absence of reaction to hind foot pinch. The surgical procedure underwent in aseptic conditions (skin preparation, sterilized instruments, gloves and drapes). Photosensitive polymers were either autoclaved (HCC-4arm PEG or HCC-8arm PEG) or 0.22 μ m filtered (HCC-Gel) before *in vivo* application. Specific working conditions used for i3D bioprinting are described in **Suppl. Table 6**. For blood flow analysis, Rhodamine B isothiocyanate–Dextran (Sigma, R9379) was injected in

Deleted: 1:100 Rabbit anti-Desmin (Sigma, D8281), 1:100 mouse anti- α -Actinin (Sigma, A7811),

tail vein at 50 mg/mL in physiologic solution. When required, skin wound was closed with Vicryl 6-0 suture and no movement or space restriction were applied to animals after treatments. At the required time point, animals were deeply anesthetized, subjected to stereomicroscope and/or 2P intravital imaging, then sacrificed for tissues collection.

5 For i3D printing into skin, intra-dermal injection of 20 μ L of HCC-4arm PEG or HCC-8arm PEG solutions (300 mg/mL in PBS) was performed at the abdomen, ear or hindlimb by using insulin syringes (Sacco, MED320924). Defined ROIs were subject to 2P irradiation across the epidermis for hydrogel crosslinking and animals analyzed after i3D bioprinting.

10 For i3D printing into muscle, a skin incision was performed to expose the epimysium of the lateral hindlimb. Then, 10 μ L of HCC-4arm PEG or HCC-8arm PEG solution (300 mg/mL in PBS) were injected between the epimysium and the skeletal muscle by using insulin syringes (Sacco, MED320924). Defined ROIs were subject to 2P irradiation for hydrogel crosslinking between the epimysium and myofibers and animals analyzed after i3D bioprinting, 4 hours or 4 days after treatment.

15 For i3D printing into brain, a skin incision was performed to expose the skull. A small window in the skull (approx. 3 mm diameter) was performed with a drill around bregma to expose the brain. Then, 4 μ L of HCC-8arm PEG solution (300 mg/mL in PBS) was injected sub-meningeal by using an Hamilton syringe connected to a glass capillary. For all the procedure, a glass coverslip was located above the site of the injection to allow objective immersion in PBS, before proceeding to i3D printing and intravital imaging.

20 For i3D bioprinting of mCherry⁺FBs, 1.4×10^4 cells were resuspended in 8 μ L of HCC-Gel and then injected sub-epidermally or between the epimysium and the skeletal muscle by using insulin syringes, then eventually processed for i3D bioprinting and analyzed 14 or 21 days after treatment.

25 For i3D bioprinting of muscular cells, a mix of 1.4×10^4 GFP⁺MuSCs and 6×10^3 mCherry⁺FBs were used (70:30⁵¹) were resuspended in 8 μ L of HCC-Gel or PBS and then injected between the epimysium and the skeletal muscle of wild-type animals by using insulin syringes, then eventually processed for i3D bioprinting and analyzed 7 days after treatment.

Image preparation and analysis.

30 We used ImageJ software for adjustments of levels and contrast, maximum and standard deviation intensity projections, 3D reconstructions and thresholding to create binary mask used for directionality and ferret angle measurements. To quantify the directionality of i3D bioprinted cells, at least 9 fluorescence images of independent biological triplicates for each sample were converted in binary masks, then analyzed with directionality plugin of ImageJ software (that indicates the amount of structures in a given direction). To quantify the shape of enclosed hSIOs, at least 9 fluorescence images of independent biological triplicates for each sample were converted in binary masks, then analyzed with measure plugin of ImageJ software to quantify the Feret's angle (the angle between the longest distance of the axis of any two points along the selection boundary (Feret's diameter) and a line parallel to the x-axis of the image).

40 All mentioned ImageJ plugins have source code available and are licensed under open-source GNU GPL v3 license.

Statistical analysis.

5

All the analysis were performed with GraphPad prism 6 software. We expressed data as means \pm s.e.m or s.d (when indicated). We determined statistical significance by unequal variance Student's t-test or one-way ANOVA and Tukey's multiple comparison test, or Kruskal-Wallis and Dunn's multiple comparison test. A *P* value of less than 0.05 was considered statistically significant.

References

1. Kruth, J. P. Material Incess Manufacturing by Rapid Prototyping Techniques. *CIRP Ann. - Manuf. Technol.* **40**, 603–614 (1991).
- 5 2. Gross, B. C., Erkal, J. L., Lockwood, S. Y., Chen, C. & Spence, D. M. Evaluation of 3D printing and its potential impact on biotechnology and the chemical sciences. *Anal. Chem.* **86**, 3240–3253 (2014).
3. Moroni, L. *et al.* Biofabrication strategies for 3D in vitro models and regenerative medicine. *Nat. Rev. Mater.* **3**, 21–37 (2018).
- 10 4. Murphy, S. V. & Atala, A. 3D bioprinting of tissues and organs. *Nat. Biotechnol.* **32**, 773–785 (2014).
5. Ong, C. S. *et al.* 3D bioprinting using stem cells. *Pediatr. Res.* 1–23 (2017). doi:10.1038/pr.2017.252
- 15 6. Kang, H. W. *et al.* A 3D bioprinting system to produce human-scale tissue constructs with structural integrity. *Nat. Biotechnol.* **34**, 312–319 (2016).
7. Hong, N., Yang, G.-H., Lee, J. & Kim, G. 3D bioprinting and its *in vivo* applications. *J. Biomed. Mater. Res. Part B Appl. Biomater.* 444–459 (2017). doi:10.1002/jbm.b.33826
8. Wang, M. *et al.* The trend towards in vivo bioprinting. *Int. J. Bioprinting* (2015). doi:10.18063/IJB.2015.01.001
- 20 9. Skardal, A. *et al.* Bioprinted Amniotic Fluid-Derived Stem Cells Accelerate Healing of Large Skin Wounds. *Stem Cells Transl. Med.* **1**, 792–802 (2012).
10. Binder, K. W. *et al.* In situ bioprinting of the skin for burns. *J. Am. Coll. Surg.* **211**, S76 (2010).
- 25 11. Keriquel, V. *et al.* In situ printing of mesenchymal stromal cells, by laser-assisted bioprinting, for in vivo bone regeneration applications. *Sci. Rep.* **7**, 1–10 (2017).
12. Di Bella, C. *et al.* In situ handheld three-dimensional bioprinting for cartilage regeneration. *J. Tissue Eng. Regen. Med.* 611–621 (2017). doi:10.1002/term.2476
13. Wang, X., Rivera-Bolanos, N., Jiang, B. & Ameer, G. A. Advanced Functional Biomaterials for Stem Cell Delivery in Regenerative Engineering and Medicine. *Advanced Functional Materials* **29**, 1–31 (2019).
- 30 14. Zhang, Z., Wang, B., Hui, D., Qiu, J. & Wang, S. 3D bioprinting of soft materials-based regenerative vascular structures and tissues. *Compos. Part B Eng.* **123**, 279–291 (2017).
15. Chin, S. Y. *et al.* Additive manufacturing of hydrogel-based materials for next-generation implantable medical devices. *Sci. Robot.* **2**, eaah6451 (2017).
- 35 16. Murphy, S. V., Skardal, A. & Atala, A. Evaluation of hydrogels for bio-printing applications. *J. Biomed. Mater. Res. - Part A* (2013). doi:10.1002/jbm.a.34326
17. König, K. Multiphoton microscopy in life sciences. *J. Microsc.* **200**, 83–104 (2000).
18. Chang, H., Shi, M., Sun, Y. & Jiang, J. Photo-dimerization characteristics of coumarin pendants within amphiphilic random copolymer micelles. *Chinese J. Polym. Sci.* **33**, 1086–1095 (2015).
- 40 19. Mahon, M. F., Raithby, P. R. & Sparkes, H. A. Investigation of the factors favouring solid state [2+2] cycloaddition reactions; the [2+2] cycloaddition reaction of coumarin-3-carboxylic acid. *Crystengcomm* **10**, 573–576 (2008).
- 45 20. Wang, D., Hou, X., Ma, B., Sun, Y. & Wang, J. UV and NIR dual-responsive self-assembly systems based on a novel coumarin derivative surfactant. *Soft Matter* **13**, 6700–6708 (2017).

21. Belfield, K. D., Bondar, M. V, Liu, Y. & Przhonska, O. V. Photophysical and photochemical properties of 5, 7-di- methoxycoumarin under one- and two-photon excitation. 69–78 (2003). doi:10.1002/poc.576
22. Iliopoulos, K., Krupka, O., Gindre, D. & Salle, M. Reversible Two-Photon Optical Data Storage in Coumarin-Based Copolymers. 14343–14345 (2010).
23. Kim, S. H., Sun, Y., Kaplan, J. A., Grinstaff, M. W. & Parquette, J. R. Photo-crosslinking of a self-assembled coumarin-dipeptide hydrogel. *New J. Chem.* **39**, 3225–3228 (2015).
24. Kabb, C. P., O'Bryan, C. S., Deng, C. C., Angelini, T. E. & Sumerlin, B. S. Photoreversible Covalent Hydrogels for Soft-Matter Additive Manufacturing. *ACS Appl. Mater. Interfaces* **10**, 16793–16801 (2018).
25. Zhu, C. & Bettinger, C. J. Light-induced remodeling of physically crosslinked hydrogels using near-IR wavelengths. *J. Mater. Chem. B* **2**, 1613–1618 (2014).
26. Azagarsamy, M. A., Mckinnon, D. D., Alge, D. L. & Anseth, K. S. Coumarin-Based Photodegradable Hydrogel: Design, Synthesis, Gelation, and Degradation Kinetics. (2014).
27. Williams, C. G., Malik, A. N., Kim, T. K., Manson, P. N. & Elisseeff, J. H. Variable cytocompatibility of six cell lines with photoinitiators used for polymerizing hydrogels and cell encapsulation. *Biomaterials* **26**, 1211–1218 (2005).
28. Torgersen, J. *et al.* Hydrogels for two-photon polymerization: A toolbox for mimicking the extracellular matrix. *Adv. Funct. Mater.* **23**, 4542–4554 (2013).
29. Xing, J.-F., Zheng, M.-L. & Duan, X.-M. Two-photon polymerization microfabrication of hydrogels: an advanced 3D printing technology for tissue engineering and drug delivery. *Chem. Soc. Rev.* **44**, 5031–5039 (2015).
30. Ingber, D. E. Cellular mechanotransduction: putting all the pieces together again. *FASEB J.* **20**, 811–827 (2006).
31. Dupont, S. *et al.* Role of YAP/TAZ in mechanotransduction. *Nature* **474**, 179–184 (2011).
32. Bian, L. *et al.* The influence of hyaluronic acid hydrogel crosslinking density and macromolecular diffusivity on human MSC chondrogenesis and hypertrophy. *Biomaterials* **34**, 413–421 (2013).
33. Brigo, L. *et al.* 3D high-resolution two-photon crosslinked hydrogel structures for biological studies. *Acta Biomater.* (2017). doi:10.1016/j.actbio.2017.03.036
34. Lefort, C. A review of biomedical multiphoton microscopy and its laser sources. *Journal of Physics D: Applied Physics* **50**, (2017).
35. Ostrovidov, S. *et al.* Skeletal Muscle Tissue Engineering: Methods to Form Skeletal Myotubes and Their Applications. *Tissue Eng. Part B Rev.* (2014). doi:10.1089/ten.teb.2013.0534
36. Moon, D. G., Christ, G., Stitzel, J. D., Atala, A. & Yoo, J. J. Cyclic Mechanical Preconditioning Improves Engineered Muscle Contraction. *Tissue Eng. Part A* (2008). doi:10.1089/tea.2007.0104
37. Gjorevski, N. *et al.* Designer matrices for intestinal stem cell and organoid culture. *Nature* **539**, 560–564 (2016).
38. Morra, M. On the molecular basis of fouling resistance. *J. Biomater. Sci. Polym. Ed.* (2000). doi:10.1163/156856200743869
39. Drumheller, P. D. & Hubbell, J. A. Densely crosslinked polymer networks of poly(ethylene glycol) in trimethylolpropane triacrylate for cell-adhesion-resistant surfaces. *J. Biomed. Mater. Res.* (1995). doi:10.1002/jbm.820290211

40. Gjorevski, N. & Lutolf, M. P. Synthesis and characterization of well-defined hydrogel matrices and their application to intestinal stem cell and organoid culture. *Nat. Protoc.* **12**, 2263–2274 (2017).
41. Kominami, K. *et al.* The molecular mechanism of apoptosis upon caspase-8 activation: Quantitative experimental validation of a mathematical model. *Biochim. Biophys. Acta - Mol. Cell Res.* **1823**, 1825–1840 (2012).
42. Bart Tummers and Douglas R Green. Caspase-8; regulating life and death. *Immunol Rev* **277**, 76–89 (2017).
43. Swartzlander, M. D., Lynn, A. D., Blakney, A. K., Kyriakides, T. R. & Bryant, S. J. Understanding the host response to cell-laden poly(ethylene glycol)-based hydrogels. *Biomaterials* (2013). doi:10.1016/j.biomaterials.2012.10.037
44. Qazi, T. H. *et al.* Cell therapy to improve regeneration of skeletal muscle injuries. *J. Cachexia. Sarcopenia Muscle* **49**, (2019).
45. Yin, H., Price, F. & Rudnicki, M. A. Satellite cells and the muscle stem cell niche. *Physiol. Rev.* **93**, 23–67 (2013).
46. Cerletti, M. *et al.* Highly Efficient, Functional Engraftment of Skeletal Muscle Stem Cells in Dystrophic Muscles. *Cell* (2008). doi:10.1016/j.cell.2008.05.049
47. Rossi, C. A. *et al.* In vivo tissue engineering of functional skeletal muscle by freshly isolated satellite cells embedded in a photopolymerizable hydrogel. *FASEB J.* **25**, 2296–2304 (2011).
48. Chapman, M. A., Meza, R. & Lieber, R. L. Skeletal muscle fibroblasts in health and disease. *Differentiation* (2016). doi:10.1016/j.diff.2016.05.007
49. Mendias, C. L. Fibroblasts take the centre stage in human skeletal muscle regeneration. *J. Physiol.* (2017). doi:10.1113/JP274403
50. Murphy, M. M., Lawson, J. A., Mathew, S. J., Hutcheson, D. A. & Kardon, G. Satellite cells, connective tissue fibroblasts and their interactions are crucial for muscle regeneration. *Development* **138**, 3625–3637 (2011).
51. Urciuolo, A. *et al.* Decellularised skeletal muscles allow functional muscle regeneration by promoting host cell migration. *Sci. Rep.* (2018). doi:10.1038/s41598-018-26371-y
52. Rossi, G., Manfrin, A. & Lutolf, M. P. Progress and potential in organoid research. *Nat. Rev. Genet.* **19**, 671–687 (2018).
53. Foster, A. A., Marquardt, L. M. & Heilshorn, S. C. The diverse roles of hydrogel mechanics in injectable stem cell transplantation. *Curr. Opin. Chem. Eng.* **15**, 15–23 (2017).
54. Hoover, E. E. & Squier, J. A. Advances in multiphoton microscopy technology. *Nat. Photonics* **7**, 93–101 (2013).
55. Horton, N. G. *et al.* In vivo three-photon microscopy of subcortical structures within an intact mouse brain. *Nat. Photonics* (2013). doi:10.1038/nphoton.2012.336
56. Oser, C. H. M. Microfabrication Through a Multimode Optical Fiber. **26**, 1766–1778 (2018).
57. Chu, W. *et al.* Centimeter-scale superfine three-dimensional printing with femtosecond laser two-photon polymerization. (2017).
58. Schultz, S. R., Copeland, C. S., Foust, A. J. & Quicke, P. Technologies for Functional Neural Circuit Imaging. 1–33 (2018). doi:10.1109/JPROC.2016.2577380. Advances
59. Horváth, O. P. Minimal invasive surgery. *Acta Chir. Hung.* **36**, 130–131 (1997).
60. Palep, J. H. Robotic assisted minimally invasive surgery. *J. Minim. Access Surg.* **5**, 1–7

- (2009).
61. Sims, G. E. C. & Snape, T. J. A method for the estimation of polyethylene glycol in plasma protein fractions. *Anal. Biochem.* **107**, 60–63 (1980).
- 5 62. Habeeb, A. F. S. A. Determination of free amino groups in proteins by trinitrobenzenesulfonic acid. *Anal. Biochem.* **14**, 328–336 (1966).
63. Natarajan, D. *et al.* Lentiviral labeling of mouse and human enteric nervous system stem cells for regenerative medicine studies. *Neurogastroenterol. Motil.* **26**, 1513–1518 (2014).
64. Urciuolo, A. *et al.* Collagen VI regulates satellite cell self-renewal and muscle regeneration. *Nat. Commun.* **4**, (2013).
- 10 65. Jung, P. *et al.* Isolation and in vitro expansion of human colonic stem cells. *Nat. Med.* **17**, 1225–1227 (2011).
66. Sato, T. *et al.* Long-term expansion of epithelial organoids from human colon, adenoma, adenocarcinoma, and Barrett’s epithelium. *Gastroenterology* **141**, 1762–1772 (2011).
- 15 67. Ajduk, A., Biswas Shivhare, S. & Zernicka-Goetz, M. The basal position of nuclei is one pre-requisite for asymmetric cell divisions in the early mouse embryo. *Dev. Biol.* **392**, 133–140 (2014).

Acknowledgments:

This work was supported by 2018 STARS-WiC grant of University of Padova, Progetti di Eccellenza CaRiPaRo, TWINING of University of Padova, Oak Foundation Award (Grant No. W1095/OCAIY-14-191) to N.E., and the STARS Starting Grant 2017 of University of Padova (Grant Code: LS3-19613) to A.U. PDC is supported by NIHR. All research at Great Ormond Street Hospital NHS Foundation Trust and UCL Great Ormond Street Institute of Child Health is made possible by the NIHR Great Ormond Street Hospital Biomedical Research Centre. The views expressed are those of the author(s) and not necessarily those of the NHS, the NIHR or the Department of Health. We thank Dr. Dale Moulding for technical support. [We thank Prof. Stefano Schiaffino for scientific advice and discussion.](#)

Author contributions:

A.U. and N.E. designed the experiments. N.E. designed the photo-chemistry, I.P. synthesized and chemically characterized the coumarin-polymers and S.S. helped with the chemical characterization of coumarin-polymers. A.U. performed and analyzed *in vitro* and *in vivo* experiments. L.B. and P.R. helped with *in vitro* experiments. V.S. helped with the analysis of *in vivo* experiments. C.L. performed hydrogel injection into the brain, derived reporter cells and hES-derived NSCs. G.G., E.Z., G.S. M.M. helped with organoid experiments. G.G. and P.D.C. characterized human intestinal organoid cultures. L.B. helped in designing and interpretation of *in vitro* two-photon crosslinking experiments. M.G. performed AFM analysis. A.U. and N.E. analyzed the data and wrote the manuscript. N.E. supervised the project. **Competing interests:** N.E. has an equity stake in ONYEL Biotech srl. A.U. and N.E. are submitting a patent for the intravitreal bioprinting. **Data and materials availability:** All data is available in the main text or the supplementary materials.

Author Affiliations:

Industrial Engineering Department, University of Padova, Italy

A.U., M.G., L.B., C.L., N.E.

Venetian Institute of Molecular Medicine, Padova, Italy

A.U., I.P., L.B., C.L., N.E.

Women's and Children's Health Department, University of Padova, Italy

A.U., E.Z., P.R., V.S.

ONYEL Biotech srl, Padova, Italy

I.P.

Department of Pharmaceutical and Pharmacological Science, University of Padova, Italy

S.S.

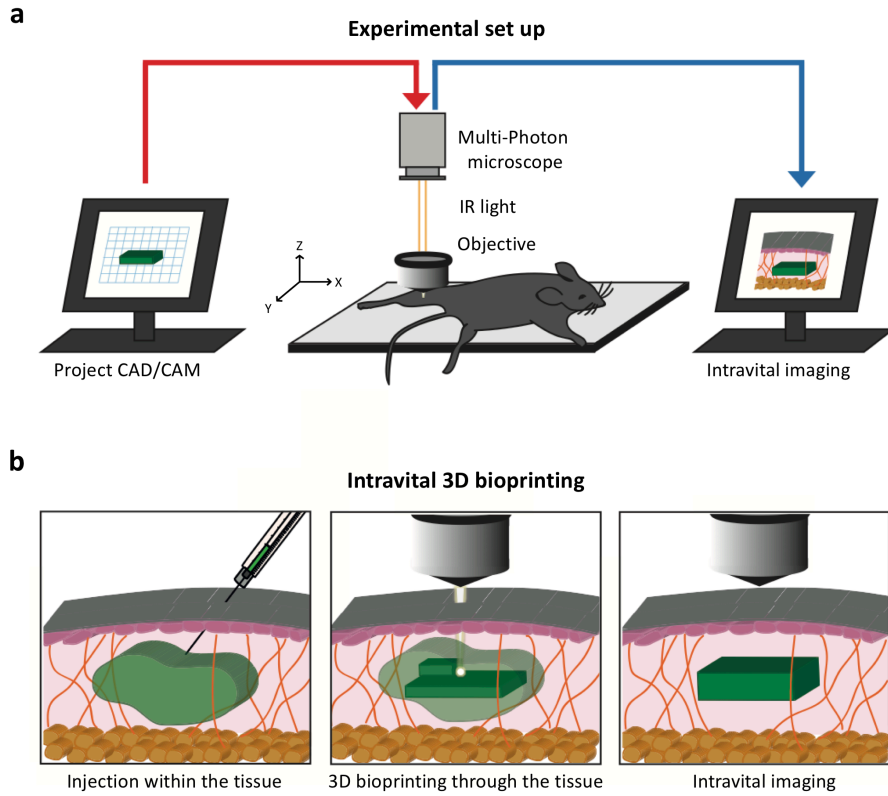
University College London ICH, London, United Kingdom

G.G., G.S., M.M., P. D.C., N.E.

Shanghai Tech University, China

N.E.

Figures and Figure legends:



5

Figure 1.

Intravital 3D bioprinting setup and *in vivo* application. **a**, Intravital 3D (i3D) bioprinting requires: a multi-photon microscope equipped with a motorized XYZ stage and a femtosecond near-IR tightly-focused pulsed laser emission. **b**, i3D bioprinting is performed by injection of HCC-polymeric solution into organs of living animals, fabrication of 3D hydrogel objects by 2P excitation, and *intravital* imaging for hydrogel identification and *in vivo* analysis.

10

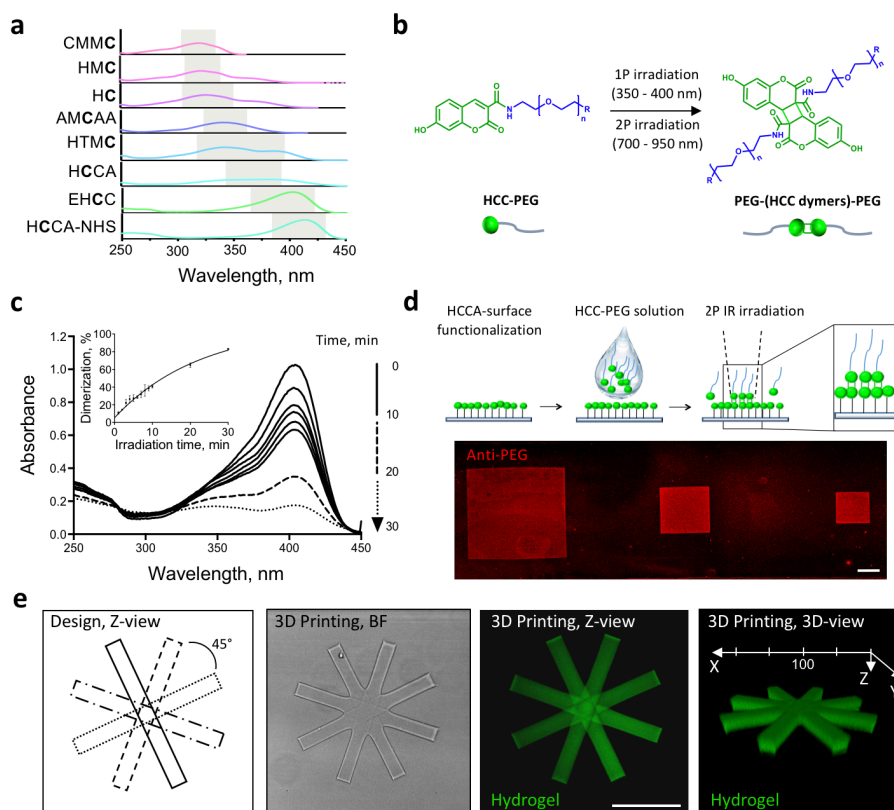
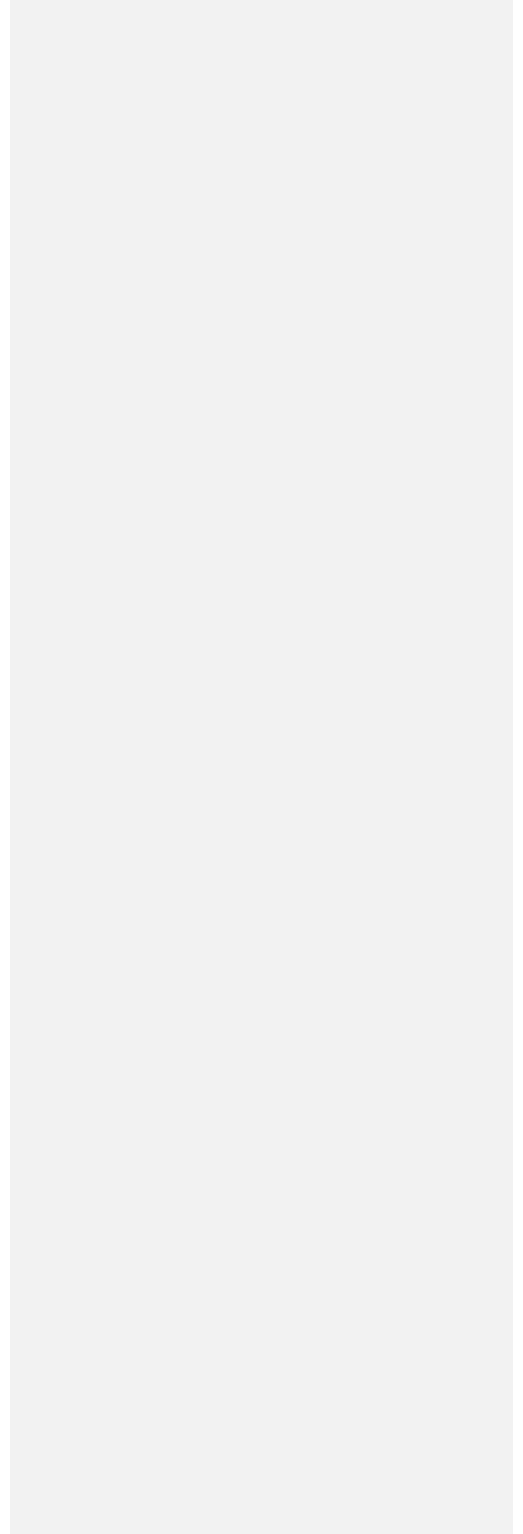


Figure 2.

- 5 **Development of injectable HCC-conjugated polymers for i3D bioprinting application.** **a**, Absorption spectra of selected coumarin derivatives (C in bold) in PBS, pH 7.4. The gray rectangle highlights the maximum absorbance peaks. HCCA-NHS, 7-Hydroxycoumarin-3-carboxylic acid N-succinimidyl ester; EHCC, Ethyl 7-Hydroxycoumarin-3-carboxylate; HCCA 7-Hydroxycoumarin-3-carboxylic acid; HTMC, 7-Hydroxy-4-(trifluoromethyl)coumarin; AMCAA, 7-Amino-4-methyl-3-coumarinylacetic acid; HC, 7-Hydroxycoumarin; HMC, 7-Hydroxy-4-methylcoumarin; CMMC, 7-Carboxymethoxy-4-methylcoumarin.
- 10 **b**, Illustration of HCC-PEG [2+2] cycloaddition reaction promoted by 1-Photon or 2-Photon irradiation. **c**, Absorbance spectra analysis showing HCC-PEG [2+2] cycloaddition after irradiation with single-photon light ($\lambda = 365$ nm) at different time points (2 min until 10 min, continuous line; 20 min, broken line; 30 min, dotted line). The inset shows HCC-PEG dimerization degree at increasing irradiation time (each min until 10 min, at 20 min, 15 and at 30 min).
- 15 **d**, Illustration of HCCA-surface functionalization and HCC-PEG 2P near-IR light-mediated cycloaddition ($\lambda = 800$ nm) within defined area of excitation, performed by multiphoton microscopy. Identification of crosslinked HCC-PEG with respect to HCC-functionalized surface was performed by immunofluorescence analysis against PEG (red). Scale bar 200 μ m. **e**, Design

and fabrication of multiple 3D parallelepipeds of HCC-Gel rotated by 45° around mass center placed on the same Z plane. Bright field and confocal Z-stack or 3D-volume reconstruction images are shown. $\Delta Z = 20 \mu\text{m}$. Scale bars 100 μm (Z-view); in 3D reconstruction XYZ coordinates and scale bar of 50 μm are shown. Specific bioprinting conditions are reported in Suppl. Table S3.

5



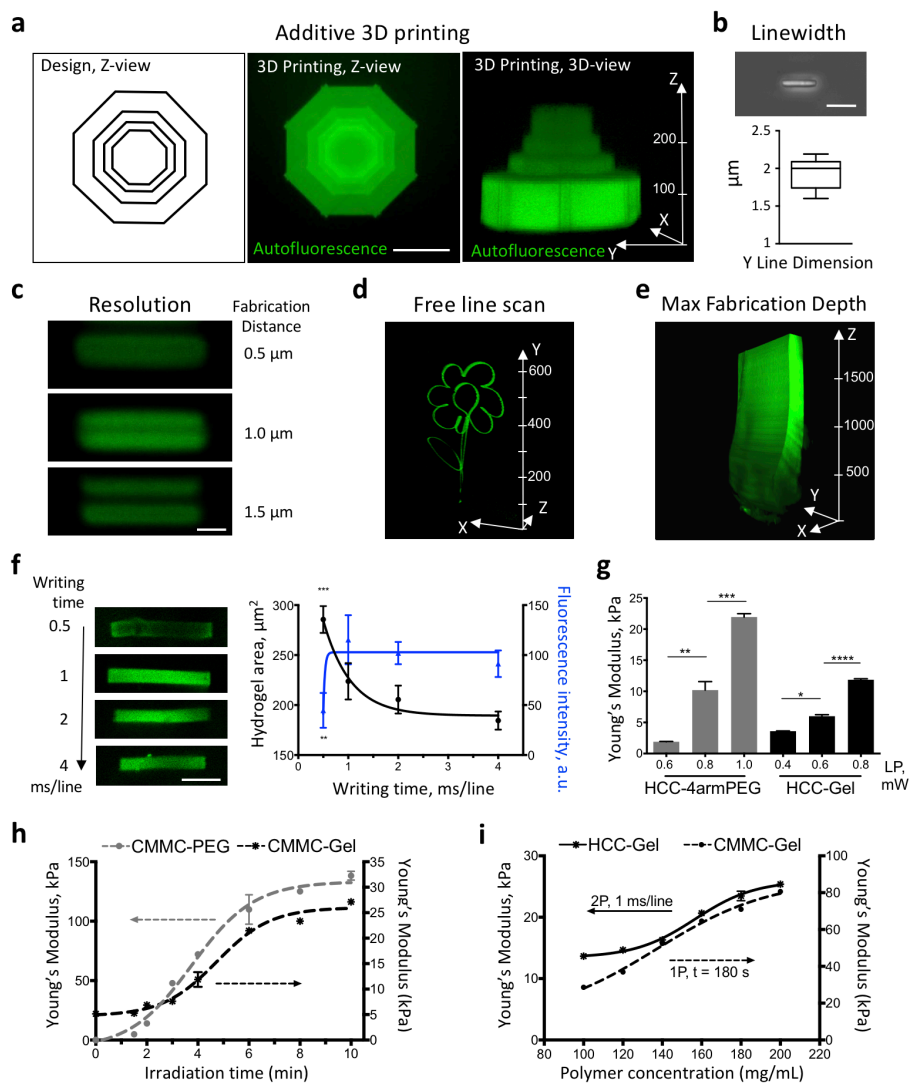


Figure 3

Characterization of the photo-sensitive polymers. **a**, Design and confocal Z-stack images of HCC-Gel objects fabricated at different Z volume positions by using near-IR laser pulses through a multiphoton microscope; total $\Delta Z = 110 \mu\text{m}$. 3D-volume reconstruction reveals the volumetric position of the multiple objects; XYZ coordinates are shown. Scale bars, 100 μm . **b**, Upper panel, representative phase-contrast

5

image of an isolated HCC-8arm PEG structure fabricated as single scan, returning the minimum linewidth achievable by the multiphoton setup. $\Delta Z = 20 \mu\text{m}$. Scale bar $10 \mu\text{m}$. Lower panel, quantification of the minimum linewidth obtained. Data are shown as mean \pm s.d. of 3 independent replicates. **c**, Multiple HCC-8arm PEG structures fabricated by near-IR multiphoton laser pulses showing the micrometric resolution of the multiphoton setup. $\Delta Z = 20 \mu\text{m}$. Scale bar $3 \mu\text{m}$. **d**, Representative 3D reconstruction of a HCC-Gel single line flower-shaped hydrogel fabricated by using free line scan program of the multiphoton microscope. $\Delta Z = 30 \mu\text{m}$. XYZ coordinates and scale bar of $50 \mu\text{m}$ are shown. **e**, Representative 3D-volume reconstruction of a HCC-8arm PEG object showing the maximum fabrication depth reached by using near-IR laser pulses through a multiphoton microscope at fixed laser power (2 mW, before objective back-aperture) and wavelength (850 nm). $\Delta Z = 2000 \mu\text{m}$. XYZ coordinates and scale bar of $500 \mu\text{m}$ are shown. **f**, Left panel, representative confocal images of HCC-Gel hydrogels (autofluorescence, green) fabricated at different writing times ($\sim 0.5, 1, 2$ and 4 ms/line). Scale bar $20 \mu\text{m}$. Right panel, quantification dimension (left Y axis, black) and autofluorescence intensity (right Y axis, blue) of HCC-Gel hydrogel photo-crosslinked by near-IR laser pulses associated to the multiphoton setup. Data are shown as mean \pm s.d. of 3 independent replicates; multiple comparison one-way ANOVA was used. $**P < 0.02$; $***P < 0.003$. Interpolation curves are reported. **g**, Young's modulus measured by atomic force microscopy of HCC-4arm PEG (gray) and HCC-Gel (black) hydrogels photo-crosslinked by using near-IR laser pulses through a multiphoton microscope at increasing laser powers (LP, mW) and fixed wavelength by using multiphoton microscopy. Data are shown as mean \pm s.d. of 3 independent replicates; multiple comparison one-way ANOVA was used; $*P < 0.05$; $**P < 0.02$; $***P < 0.003$; $****P < 0.001$. Specific fabrication conditions are reported in Suppl. Table S3. **h**, Young's modulus measured by atomic force microscopy of CMMC-4arm PEG (CMMC-PEG, dashed gray line, left Y axis) or CMMC-Gel (dashed black line, right Y axis) photo-crosslinked with a 365 nm UV LED at fixed working distance and increasing irradiation time. Interpolation curves are reported. Specific fabrication conditions are reported in Methods section. **i**, Young's modulus measured by atomic force microscopy of HCC-Gel (continuous line, left Y axis) or CMMC-Gel (dashed line, right Y axis) at increasing polymer concentration. HCC-Gel was photo-crosslinked by using near-IR laser pulses through a multiphoton microscope (2P) at fixed laser power (0.7 mW) and at 1 ms/line writing time. Specific fabrication conditions are reported in Suppl. Table S3. CMMC-Gel was photo-crosslinked with a 365 nm UV LED at fixed working distance and at 10 min irradiation time. Interpolation curves are reported. Specific fabrication conditions are reported in Methods section.

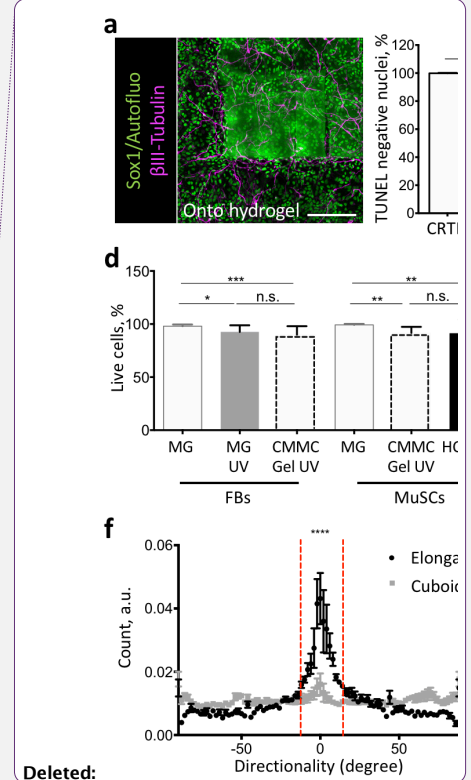
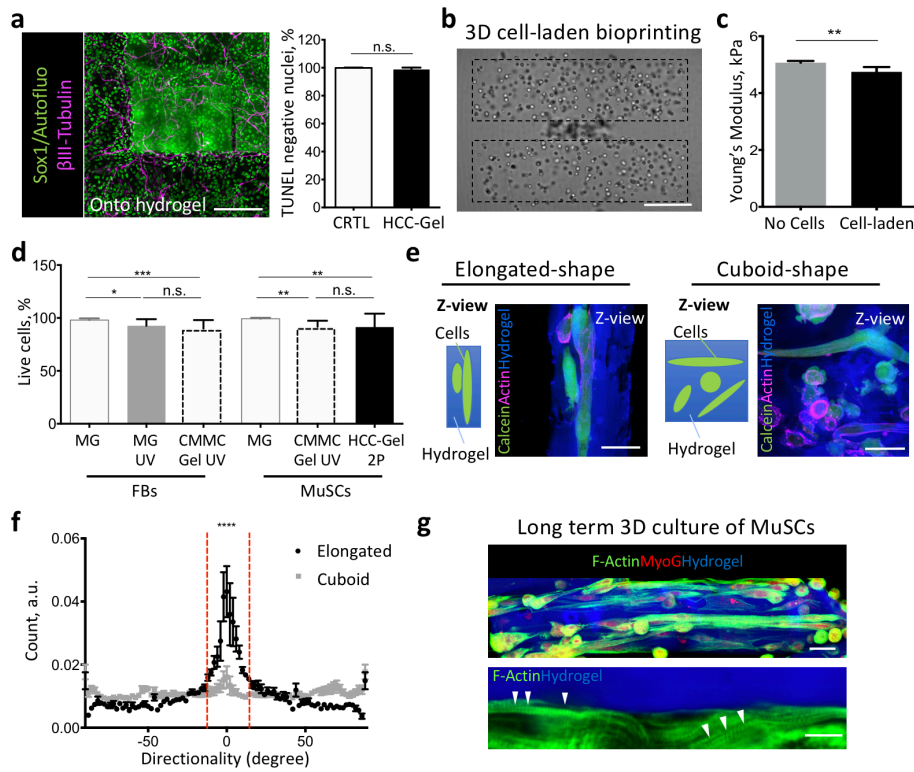


Figure 4

3D objects of photo-sensitive Gel hydrogels can be used for *in vitro* cell culture. **a**, Left panel, immunofluorescence analysis for Sox1 (green) and β -III Tubulin (magenta) of hES-derived NSC cultured for 3 days onto fabricated HCCA-Gel hydrogel structures coated with poly-L-ornithine/laminin (onto hydrogel). Scale bars, 200 μ m. Right panel, quantification of non-apoptotic hES-derived NSCs (TUNEL negative), expressed as percentage of total nuclei, cultured for 3 days onto poly-L-ornithine/laminin coated glass (CTRL) or onto fabricated HCCA-Gel hydrogel structures coated with poly-L-ornithine/laminin (HCC-Gel). Data are shown as mean \pm s.d.; n.s., not statistically significant. **b**, Representative image of a cell-laden HCC-Gel structure 6 hours after fabrication. Scale bars, 75 μ m; BF, bright field. **c**, Young's modulus of HCC-Gel (No cells) or mFB-laden HCC-Gel (cell-laden) structures measured by atomic force microscopy photo-crosslinked at identical laser power (500 mW) and fixed wavelength (800 nm) by using multiphoton microscopy. Data are shown as mean \pm s.d. of 3 independent replicates; unequal variance Student's t-test was used; * P < 0.002. **d**, Quantification of mFB or MuSC survival suspended in Matrigel (MG), Matrigel exposed to UV (MG UV), CMMC-Gel crosslinked by UV light or HCC-Gel 2P crosslinked and cultured for 48 hrs. Data are shown as mean \pm s.d. of 3 independent replicates; multiple comparison one-way ANOVA was used; n.s., not statistically significant, * P < 0.02; ** P < 0.003; *** P < 0.001. **e**, MuSCs

orientation into a cuboid- or parallelepiped elongated-shaped HCC-Gel cell-laden construct after 2 days of culture. Schematic illustration and representative fluorescence imaging showing Z-stack reconstruction (middle panel) or 3D reconstruction (left panel) of MuSC-laden HCC-Gel cuboid or parallelepiped constructs stained with calcein (green) and phalloidin (magenta). Nuclei were stained with Hoechst (blue). Scale bars, 50 μm (cuboid) or 25 μm (elongated). **f.** Quantification of cell directionality of MuSCs 3D bioprinted into parallelepiped-shaped HCC-Gel (Elongated; black) or into cuboid-shaped HCC-Gel (Cuboid; grey) 2 days after printing. **g.** Upper panel, immunofluorescence performed for F-actin (green) and myogenin (MyoG, red) of myogenic cells at 10 days of cell culture. Lower panel, higher magnification of F-actin (green) staining, in which sarcomeric organization is detectable (arrowhead). Hydrogel was revealed by autofluorescence (blue). Scale bars 10 μm . Specific bioprinting conditions are reported in Suppl. Table S4.

Deleted: Bright field (BF) and immunofluorescence images showing myogenic cells derived from MuSCs cultured on 3D parallelepiped-shaped HCC-Gel. **g.** Immunofluorescence was performed for desmin (green), alpha-actinin (red), actin (magenta). Scale bars 50 μm . Nuclei were stained with Hoechst (blue). Specific bioprinting conditions are reported in Suppl. Table S4.

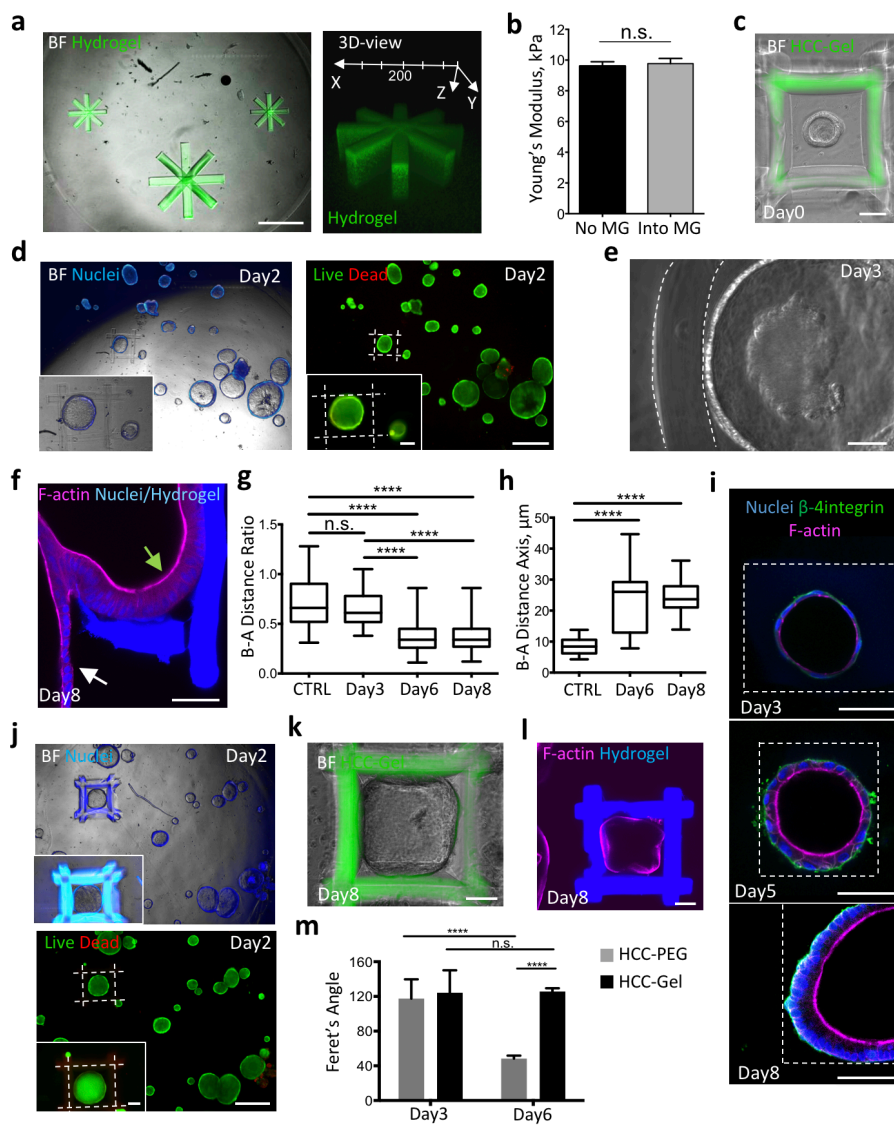


Figure 5.

HCC-Gel hydrogels can be fabricated into pre-existing 3D environment and are suitable for 3D *in vitro* human small intestinal organoid culture. **a**, Left panel, representative images of objects fabricated

5

into a drop of Matrigel. BF, bright field. Scale bar 400 μm . Right panel, 3D-volume reconstruction of the object located into the gel; $\Delta Z = 100 \mu\text{m}$. XYZ coordinates and scale bar of 100 μm are shown. **b**, Young's modulus of HCC-Gel structures fabricated outside (black, No MG) or into a Matrigel drop (white, into MG) measured by atomic force microscopy. Hydrogels were photo-crosslinked at identical laser power (500 mW) and fixed wavelength (800 nm) by using multiphoton microscopy. Data are shown as mean \pm s.d. of 3 independent replicates; unequal variance Student's t-test was used; n.s., not statistically significant. **c**, Bright field (BF) and fluorescent merged images showing hSIO cultured in Matrigel, enclosed by HCC-Gel structures after hydrogel photo-crosslinking. $\Delta Z = 300 \mu\text{m}$. Scale bar 50 μm . **d**, Representative bright field (BF) and fluorescent images displaying live (green, calcein stained) and dead (red, ethidium homodimer-1 stained) cells in hSIO cultures 2 days after HCC-Gel hydrogel 2P-crosslinking. Scale bar 400 μm . The inset shows higher magnification of the organoid enclosed into the HCC-Gel hydrogel structure. Scale bar 50 μm . $\Delta Z = 300 \mu\text{m}$. Dashed lines indicate the hydrogel position. **e**, Representative images showing the morphology of a hSIO enclosed by HCC-Gel 3D printed structures after 3 days in culture. Hydrogel was deformed by the organoid. Dashed lines indicate the position of hydrogel walls. Scale bar 50 μm . **f**, Fluorescence confocal image showing F-actin (magenta) organization of human small intestinal organoids after 8 days of cell culture. The green arrow points at a hSIO enclosed in HCC-Gel hydrogel (blue). The white arrow points at a close organoid that was not enclosed by the hydrogel. Nuclei were stained with Hoechst (blue). Scale bar 50 μm . **g**, Quantification of nuclear basal-apical (B-A) distance ratio of human small intestine organoids in standard culture condition (CTRL) or enclosed by Matrigel/HCC-Gel hydrogels at day 3, 6 and 8 of cell culture. Data are shown as mean \pm s.d. of 3 biological independent replicates; multiple comparison one-way ANOVA was used; n.s., not statistically significant; ****P < 0.0001. **h**, Quantification of the major basal-apical (B-A) axis length of hSIO in standard culture condition (CTRL) or enclosed by Matrigel/HCC-Gel hydrogels at day 6 and 8 of cell culture. Data are shown as mean \pm s.d. of 3 independent replicates; multiple comparison one-way ANOVA was used; n.s., not statistically significant; ****P < 0.0001. **i**, Immunofluorescence analysis for β -4 integrin (green) and F-actin (magenta) performed in hSIO enclosed in Matrigel/HCC-Gel hydrogels at day 2, 5 and 8 of cell culture. Dashed lines indicate the hydrogel position. Scale bar 25 μm . **j**, Representative bright field (BF) and fluorescent images displaying live (green, calcein stained) and dead (red, ethidium homodimer-1 stained) cells in hSIO cultures 48 hrs after Matrigel/HCC-8arm PEG hydrogel photo-crosslinking. Scale bar 400 μm . The inset show higher magnification of the organoid enclosed into the Matrigel/HCC-PEG hydrogel structure. Scale bar 50 μm . $\Delta Z = 300 \mu\text{m}$. BF, bright field. Dashed lines indicate the hydrogel position. **k**, Representative images showing the morphology of a hSIO enclosed in HCC-PEG 3D printed structures after 8 days in culture. Scale bar 50 μm . **l**, Fluorescence imaging showing actin (magenta) localization and hydrogel localization of a hSIO enclosed by HCC-8arm PEG 3D printed structures after 8 days in culture. Nuclei were stained with Hoechst (blue). Scale bar 50 μm . **m**, Feret's angle quantification of hSIO enclosed by HCC-8arm PEG (black) or by HCC-Gel (gray) 2 and 5 days after hydrogel bioprinting. Data are shown as mean \pm s.d. of 3 independent replicates; multiple comparison one-way ANOVA was used; n.s., not statistically significant; ****P < 0.0001. Specific bioprinting conditions are reported in Suppl. Table S5.

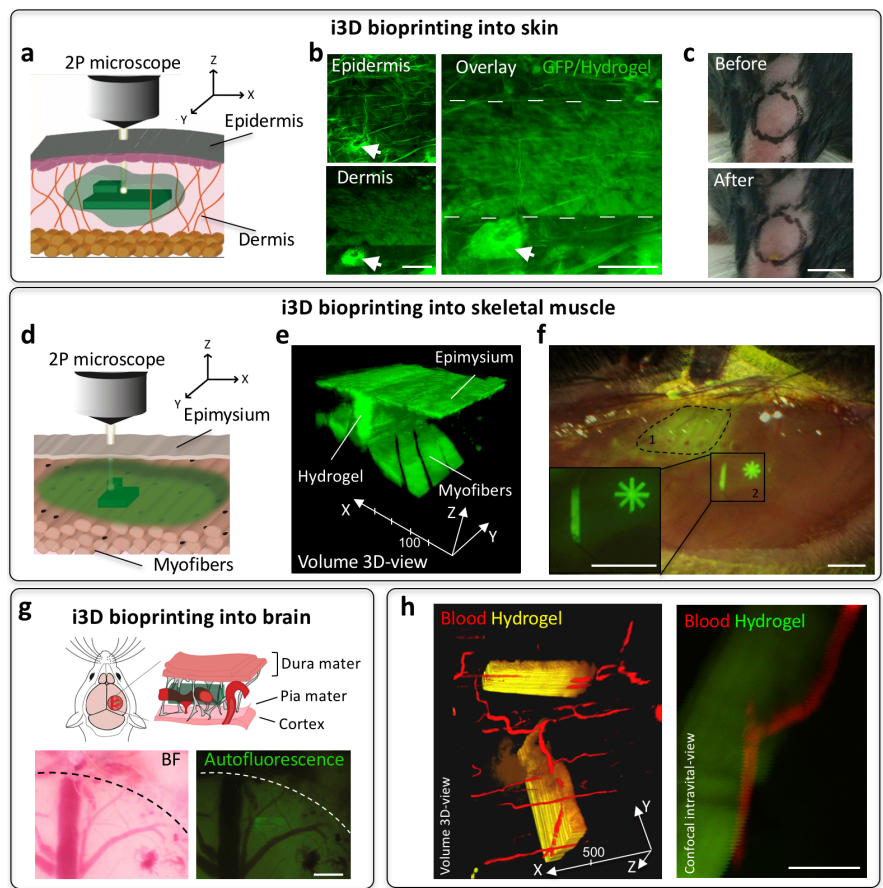


Figure 6.

Intravital 3D bioprinting. **a**, Schematic illustration showing 2P-crosslinking of HCC-hydrogel into dermis across epidermis. **b**, Representative *intravital* imaging displaying integrity of epithelial cells of epidermis and HCC-8arm PEG object fabricated into dermis (green, $\Delta Z = 100 \mu\text{m}$) of the skin in GFP⁺ animals. Dotted line in overlay panel shows the margins of the hydrogel. Arrow marks the hair bulb. Scale bars 100 μm . **c**, Representative images of hindlimb skin before and after i3D bioprinting across epidermis. Scale bar 0.5 cm. **d**, Schematic illustration showing 2P-crosslinking of HCC-hydrogel into skeletal muscle across epimysium. **e**, Representative 3D-volume reconstruction of HCC-8arm PEG structure ($\Delta Z = 300 \mu\text{m}$) manufactured between undamaged myofibres and epimysium of skeletal muscle in GFP⁺ animals; XYZ coordinates and scale bar of 50 μm are shown. **f**, Bright field and fluorescence stereomicroscope image showing injected HCC-Gel under epimysium that did not (dotted line, 1) or underwent to hydrogel photo-crosslinking (continuous line, 2). The inset is showing a higher magnification of fabricated structures. Scale bars 1 mm. **g**, Illustration and stereomicroscope images showing HCC-8arm PEG object (green, $\Delta Z = 500$

Formatted: Font: Not Bold

Formatted: Font: Not Bold

Formatted: Font: Not Bold

Formatted: Font: Not Bold

5 μm) fabricated between *dura* and *pia* mater into the brain of wild-type mice. Dotted line shows the margins of the burr-hole preformed into the skull. BF, bright field. Scale bars 850 μm . **h**, Left panel, representative 3D-volume reconstruction of HCC-8arm PEG structures (yellow, $\Delta Z = 300 \mu\text{m}$) respectively positioned at 90° and manufactured across epimysium of skeletal muscle in wild-type animals. The integrity of the blood flow is shown in red. Right panel, representative confocal *intravital* image revealing blood flow persistence inside the microvasculature embedded into the photo-crosslinked hydrogel across epimysium. Scale bar 100 μm . Specific bioprinting conditions are reported in Suppl. Table S6.

Formatted: Font: Not Bold

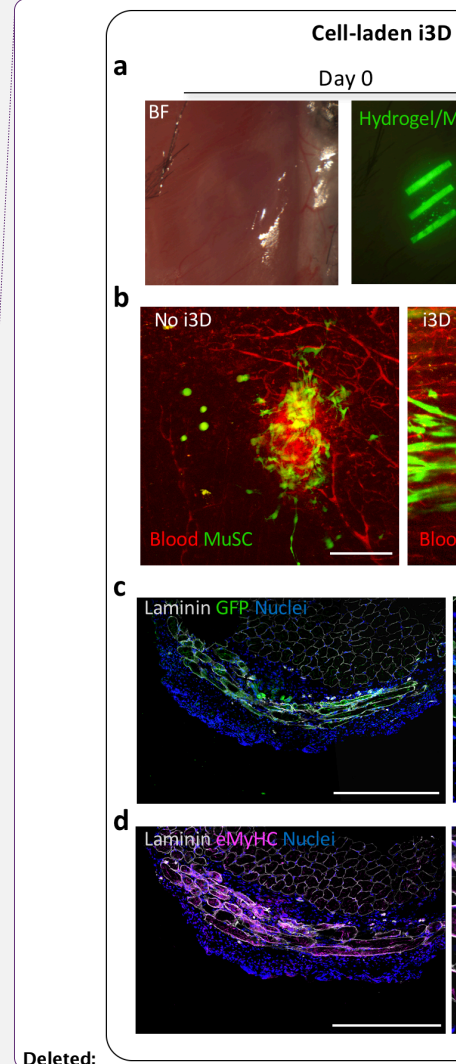
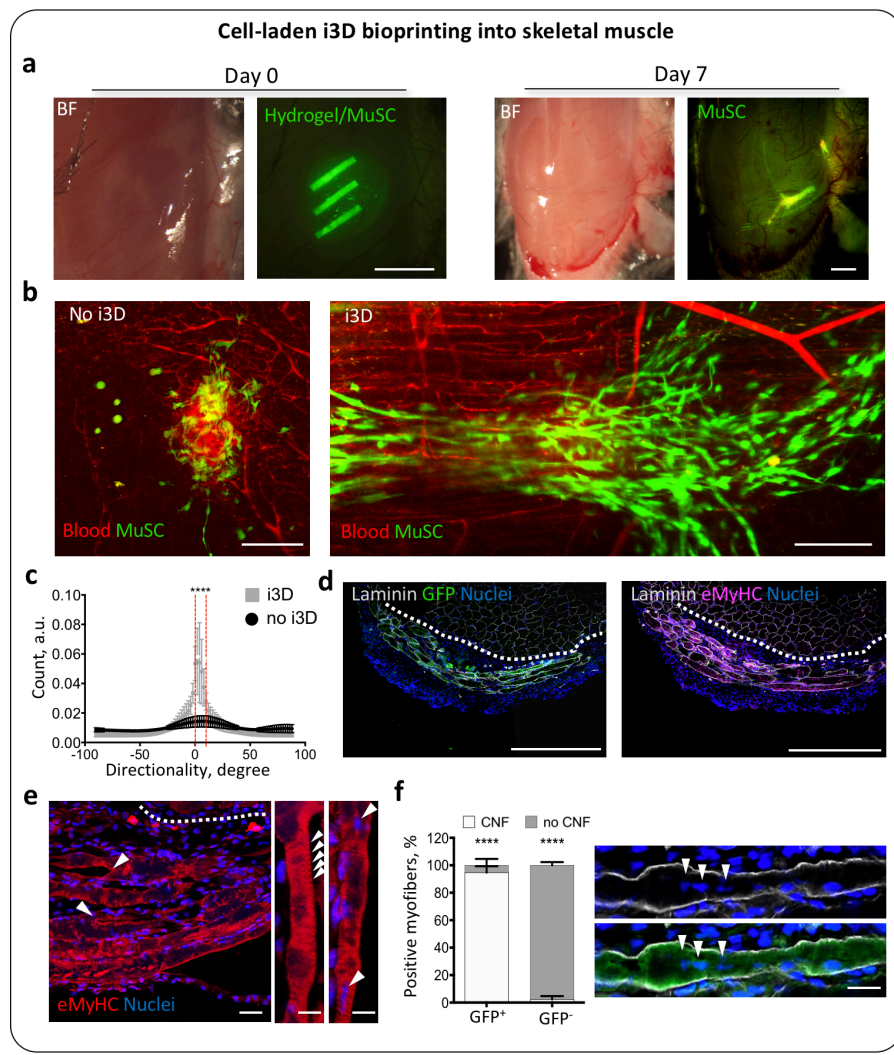


Figure 7.

Cell-laden i3D bioprinting. **a**, Representative stereomicroscope images of hindlimb muscle just after (day 0) or 7 days after i3D bioprinting across epimysium of parallelepiped-shaped GFP+MuSC/mCherry+FB HCC-Gel construct into wild-type animals. Scale bar 1mm. **b**, Intravital 2-Photon mosaic image showing GFP+MuSC-derived cells 7 days after injection under the epimysium (no i3D) or 7 days after injection and fabrication of parallelepiped-shaped GFP+MuSC(green)/mCherry+FB-laden HCC-Gel

Formatted: Font: Not Bold

Formatted: Font: Not Bold

Formatted: Font: Not Bold

5
10
15
20

construct (i3D) into wild-type animals. Blood flow is shown in red. Scale bar 200 μm . **c.** Quantification of cell directionality of GFP+ cells in i3D bioprinted muscles (gray) or in muscles injected with GFP+MuSC (black). Data are shown as mean \pm s.d. of 3 independent replicates; multiple comparison one-way ANOVA was used; ****P< 0.0001. Specific bioprinting conditions are reported in Suppl. Table S6. **d.** Mosaic images showing host and de novo tissue sections. Left panel, immunofluorescence performed for GFP (green) and laminin (gray) in wild-type animals 7 days after i3D bioprinting of GFP+MuSC/mCherry+FB-laden HCC-Gel. Right panel, immunofluorescence performed for embryonic myosin heavy chain (eMyHC, magenta) and laminin (gray) in wild-type animals 7 days after i3D bioprinting of GFP+MuSC/mCherry+FB-laden HCC-Gel. Dotted line shows the limit between host muscle (above) and de novo tissue (below); scale bars, 400 μm . Nuclei were stained with Hoechst (blue). **e.** Confocal images of regenerating myofibers stained for eMyHC. Left panel, dotted line shows the limit between host muscle (above) and de novo tissue (below). Arrowheads point at myofiber branching (left), striated organization of the cytoskeleton (middle) and presence of centrally located nuclei; scale bars, 30 μm (left) and 15 μm (middle, right). Nuclei were stained with Hoechst (blue). **f.** Left panel, quantification of GFP-negative (GFP-) and GFP-positive (GFP+) myofibers that showed centrally located nuclei (CNF) or peripheral location of the nuclei (no CNF). Data are shown as mean \pm s.d. of 3 independent replicates; multiple comparison one-way ANOVA was used; ****P< 0.0001. Right panel, representative confocal image showing multinucleated GFP+ myofibers surrounded by laminin; centrally located nuclei are highlighted by arrowheads. Scale bar 10 μm . Nuclei were stained with Hoechst (blue).

Formatted: Font: Not Bold

Formatted: Font: Not Bold

Formatted: Font: Not Bold, Superscript

Formatted: Font: Not Bold

Formatted: Font: Not Bold

Formatted: Font: Not Bold

Deleted: Cell-laden i3D bioprinting. **a.** Representative stereomicroscope images of hindlimb muscle just after (day 0) or 7 days after i3D bioprinting across epimysium of parallelepiped-shaped GFP+MuSC/mCherry+FB HCC-Gel construct (green) into wild-type animals. Scale bar 1mm. **b.** Intravital 2-Photon mosaic image showing GFP+MuSC-derived cells 7 days after injection under the epimysium (no i3D) or 7 days after injection and fabrication of parallelepiped-shaped GFP+MuSC(green)/mCherry+FB-laden HCC-Gel construct (i3D) into wild-type animals. Blood flow is shown in red. Scale bar 200 μm . **c.** Mosaic image showing immunofluorescence performed for GFP (green) and laminin (gray) on cross-section derived from wild-type animals 7 days after i3D bioprinting of GFP+MuSC/mCherry+FB-laden HCC-Gel; scale bar, 400 μm . **d.** Mosaic image showing immunofluorescence performed for embryonic myosin heavy chain (eMyHC, magenta) and laminin (gray) on cross-section derived from wild-type animals 7 days after i3D bioprinting of GFP+MuSC/mCherry+FB-laden HCC-Gel; scale bar, 400 μm . **e.** Left panel, representative confocal image showing multinucleated GFP+ myofibers surrounded by laminin; centrally located nuclei are highlighted by arrows. Scale bar 25 μm . Right panel, quantification of GFP-negative (GFP-) and GFP-positive (GFP+) myofibers that showed centrally located nuclei (CNF) or peripheral location of the nuclei (no CNF). Data are shown as mean \pm s.d. of 3 independent replicates; multiple comparison one-way ANOVA was used; ****P< 0.0001. **f.** Quantification of cell directionality of GFP+ cells in i3D bioprinted muscles (gray) or in muscles injected with GFP+MuSC (black). Data are shown as mean \pm s.d. of 3 independent replicates; multiple comparison one-way ANOVA was used; ****P< 0.0001. Specific bioprinting conditions are reported in Suppl. Table S6.